UCRL CR 105052

MRC/ABQ-R-1208
Revised October 1989
Copy 17

Mission Research Corporation

SIMULATION AND THEORY OF RADIAL EQUILIBRIUM OF PLASMOID PROPAGATION, FINAL REPORT

Mark M. Campbell
Randy M. Clark
Michael A. Mostrom

September 1989

Prepared for: Lawrence Livermore National Laboratory
Post Office Box 808
Livermore, CA 94550

Received by OSTI
OCT 1 5 1990

Under Contract: B052997

Prepared by: MISSION RESEARCH CORPORATION
1720 Randolph Road, SE.
Albuquerque, NM 87106-4245

DISTRIBUTION OF THIS DOCUMENT IS UNLIMITED

UCRL-CR--105052

DE91 000803

ABSTRACT

Cases simulating beam currents to about 29 MA were done. Significant noise reduction and code speed-up were achieved for these cases. The net current scaling observed at lower beam current ($I_{net} \sim I_{beam}^{1/2}$) continued to hold up well, as did the equilibrium itself. A slight deviation in the expected thickness and radial structure of the current layer was observed, however. A laminar flow model is developed that appears to give good agreement with the simulation results. Suggestions for future work are discussed briefly.

CONTENTS

FIGURES

1.0 INTRODUCTION

Using our earlier test data (reproduced in Appendix A), in order to reduce noise in the high-current cases we increased the number of particles per cell to 375 for the sheath, used radial current smoothing over three adjacent cells and eliminated current inside the axial cell ($R \sim 0$) to reduce the fictitious spike near the axis. This decreased the fluctuation amplitude by about a factor of three and made estimation of the average current values from the plots much easier.

The summary plots shown here are in the same format as those in Appendix A but continue the beam-current analyzed on to much higher levels. The trends are essentially as expected.

We have completed a laminar-flow equilibrium model that predicts the radial profile of the axial velocity of electrons and the relationship between azimuthal magnetic field and radial electric field. Specific predictions are obtained for the net current and ion-beam temperature necessary for equilibrium. In all cases the agreement between the model predictions and the ISIS simulations is excellent. The model also predicts parameter scalings which have not yet been tested in the simulations and, therefore, need further verification.

2.0 RESULTS OF 1.8–28.8 MA SIMULATIONS

Table 1 describes the simulation parameters and selected results for the new runs carried out in August 1989. We have also included a few older simulations that are used in some of the summary plots. In all these runs, the axial velocity of the ion beam was $\beta_{zi} = 0.62$, the annulus between the beam and the conducting pipe wall was filled with plasma at five times the beam density, and the ion beam temperature was $T_i = 43.2$ kV (the same as concluded at the end of the research in Ref. 1).

Cases were run at 1.8 MA for both a normal configuration and one with the uninteresting inner region of the beam, which usually shows (nearly) zero net current, replaced with a particle reflecting metal boundary at $R = 25$ cm (see Figs. 1–5). These cases agreed within ~ 10 percent, so higher currents were run with this feature which decreases the simulations time by about 40 percent. Because the CPU run time to steady state for the net current increases roughly as the square root of the beam current, we were able to run the 7.2 MA and 28.8 MA cases readily (Figs. 6–9 and 10–13, respectively) but a 115 MA case (which might require 15–20 CPU hours) was not undertaken due to the cost. The width of the nonzero net current region, which had previously scaled above 100 kA as approximately $\sim I_{beam}^{-1/2}$, continues its rapid decrease for $I_{beam} \gtrsim 7$ MA, (Figs. 4, 5, 9, and 13). The radial current profiles of these and some lower current cases run previously are superimposed in Fig. 14. All cases continued to exhibit approximately the same net current scaling ($I_{net} \sim I_{beam}^{1/2}$, Figs. 15–17) as observed at lower currents.

The radial structure of the sheath region is more complex than earlier thought. Noise in earlier runs masked this structure. A negative current region at the inside edge of the sheath (e.g., Fig. 14, 1.8–18.8 MA) became more obvious at higher currents. This region is a local over-neutralization of the current at the edge of the beam electrons. The sheath electron cyclotron orbit about B_θ imparts a large axial velocity component. At its innermost radial position there is some overlap with original beam electrons which have not yet been lost to the wall (see Fig. 21). Also, the sheath electrons at their inner radial position overneutralize the beam charge, form a virtual cathode (reverses the sign of E_r), and loose all their energy (Figs. 21a, c, and e). In this "mixing" region the sheath electrons lose energy and axial momentum and the original beam electrons gain it (see Fig. 21d–f).

The complicated phase space of the beam electrons (Figs. 21b, d, and f) as they leave radially is due to the field reversal of E_r and B_θ in the sheath region just inside the beam edge. E_r and B_θ have very similar radial profiles and go to zero at the same radial position (Figs. 1 and 2, 6 and 7, and 10 and 11).

No significant compression or expansion of the ion beam was observed in any of these runs, so we postulate that the equilibrium ion-beam temperature is relatively independent of current.

Figures 18–20 show that a steady state has been reached at least in the net current. The noise has been substantially reduced over the level observed in the earlier simulations reported on in Appendix A.

TABLE 1. SIMULATION RESULTS AND PARAMETERS.

LLNL Plasmoid Propagation Results August 1989

Run ID	I_b	Cell Size (cm)	X2MIN	X2MAX	Number Radial Cells
AA	1.8 MA	0.1	-0.05	53.25	533
AB	1.8 MA	0.1	25	51.8	268
AC	7.2 MA	0.05	25	50.25	505
AD	28.8 MA	0.025	25	50.25	1010
AL	22.5 kA	Run done at AFWL Aug–Oct 1988			
BE	452 kA	Run done at AFWL Aug–Oct 1988			
BB	1.8 mA	Run done at AFWL Aug–Oct 1988			

Net Current Results at Different Radius Positions

	Run ID						
Radius	AL	BE	BB	AA	AB	AC	AD
54	10.96	-3.99	-35.14				
52.8				-9.57			
51			40.17				
50.3					56.16		
50.125							-23.38
50				67.84		93.97	
49					99.77	191.58	372.52
48	10.99	41.05	95.87	86.1			
47.75							67.15
47.7						97.81	
47.5					75.34	76.3	36.53
44			35.1	11.51			
40	9.02	12.1	10.82	-20.8			
30					-0.67	-1.78	6.01
28	4.06	-1.11		-1.73			
16	0.96	-9.8					
0.6		-0.02	0.15	-0.03			

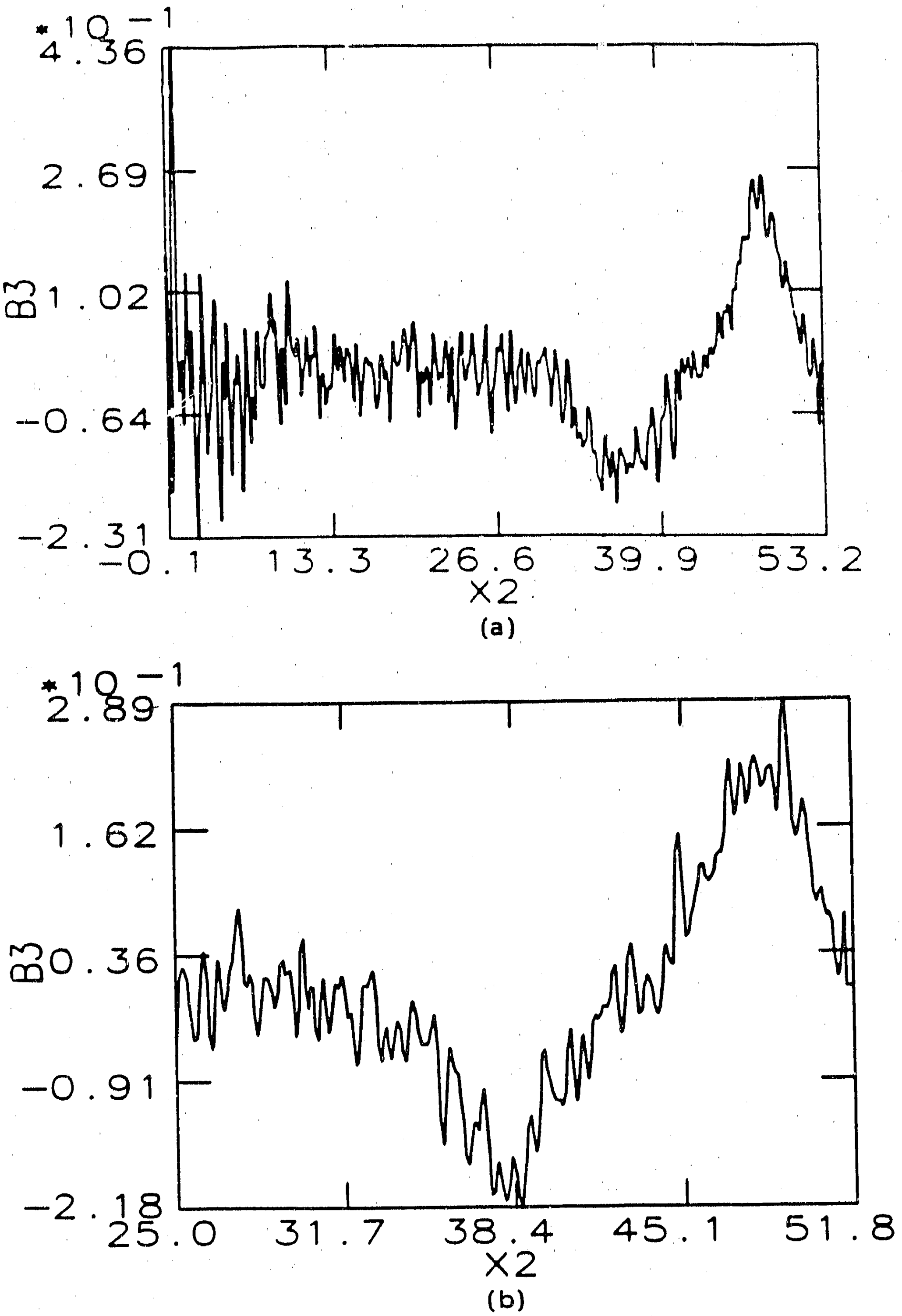

Figure 1. Periodic simulation results comparing azimuthal magnetic field B_θ (B3, 0.6 kG) versus radial position X2 = R (X2, cm) at ct = 400 cm for two runs with $I_b = 1.8$ MA. (a) run AA, (b) run AB (hollow beam), NOTE CHANGE IN X2 SCALING.

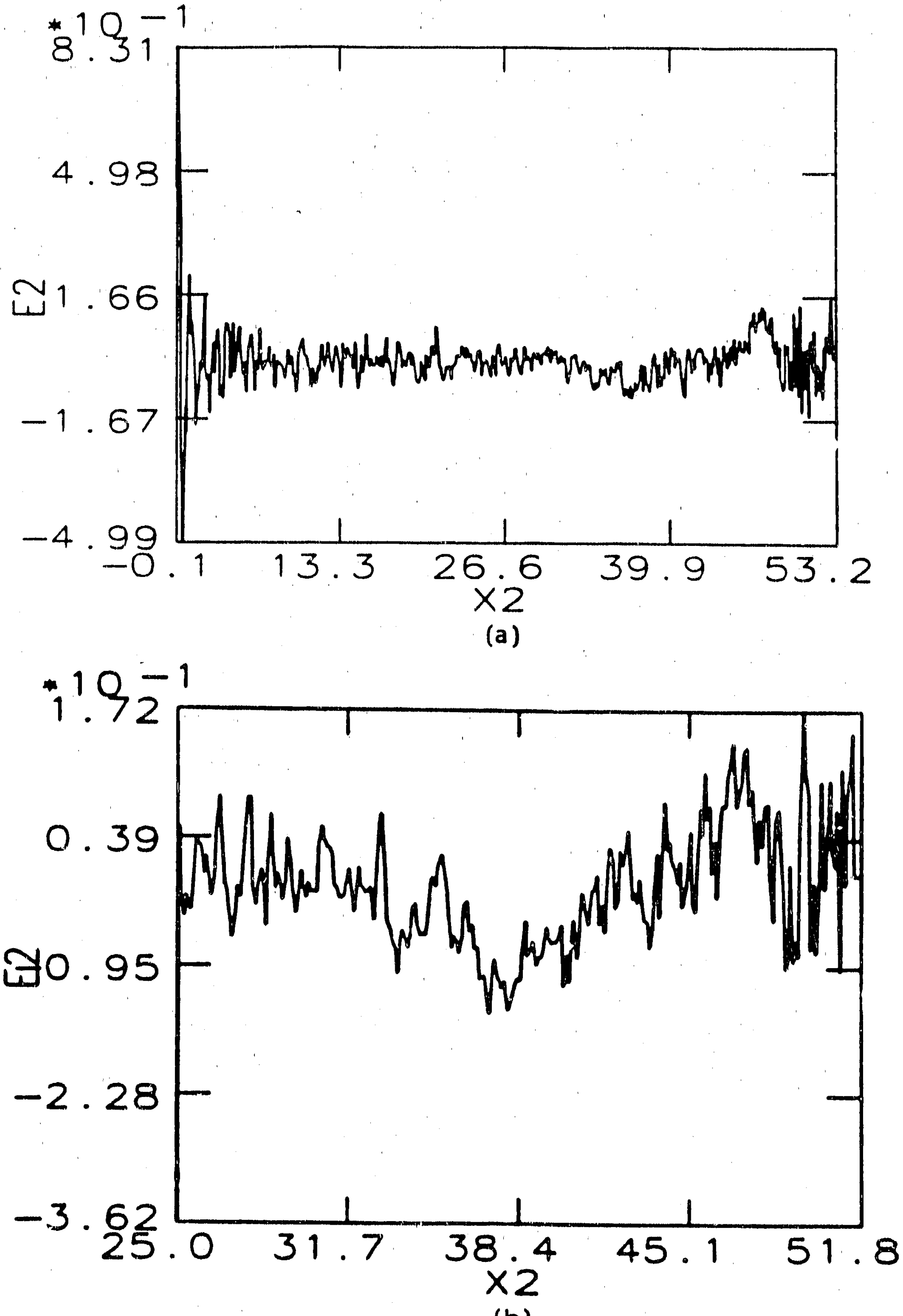

(a)

(b)

Figure 2. Periodic simulation results comparing E_r (E2, 0.51 MeV/cm) versus R (X2, cm) at ct=400 cm for two runs with $I_b = 1.8$ MA. (a) run AA, (b) run AB (hollow beam), NOTE CHANGE IN X2 SCALING.

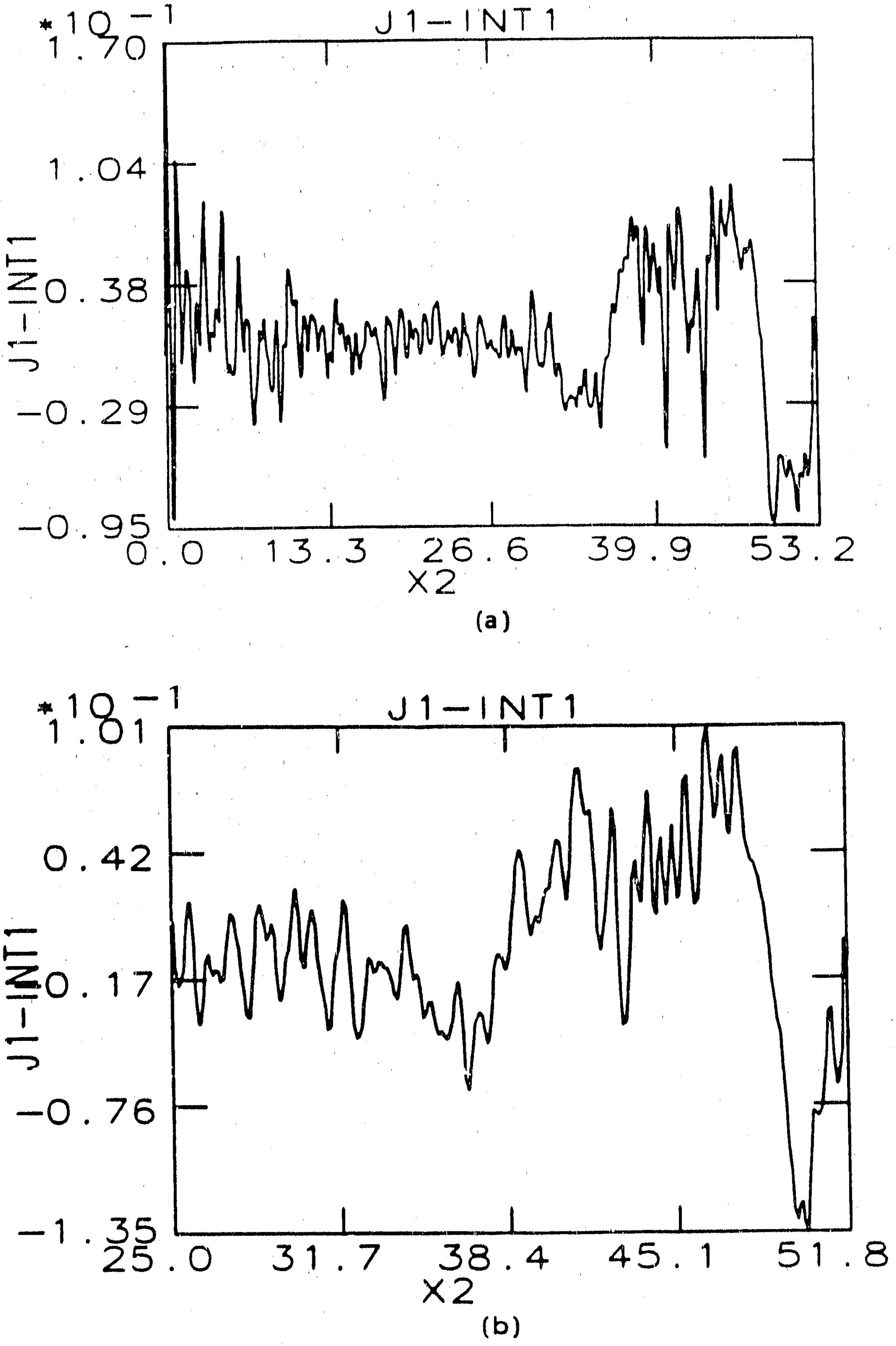

Figure 3. Periodic simulation results comparing axially-integrated J_z versus R (X2, cm) at $ct = 400$ cm for two runs with $I_b = 1.8$ MA. (a) run AA, (b) run AB (hollow beam), NOTE CHANGE IN X2 SCALING.

LLNL PLASMOID PROPAGATION

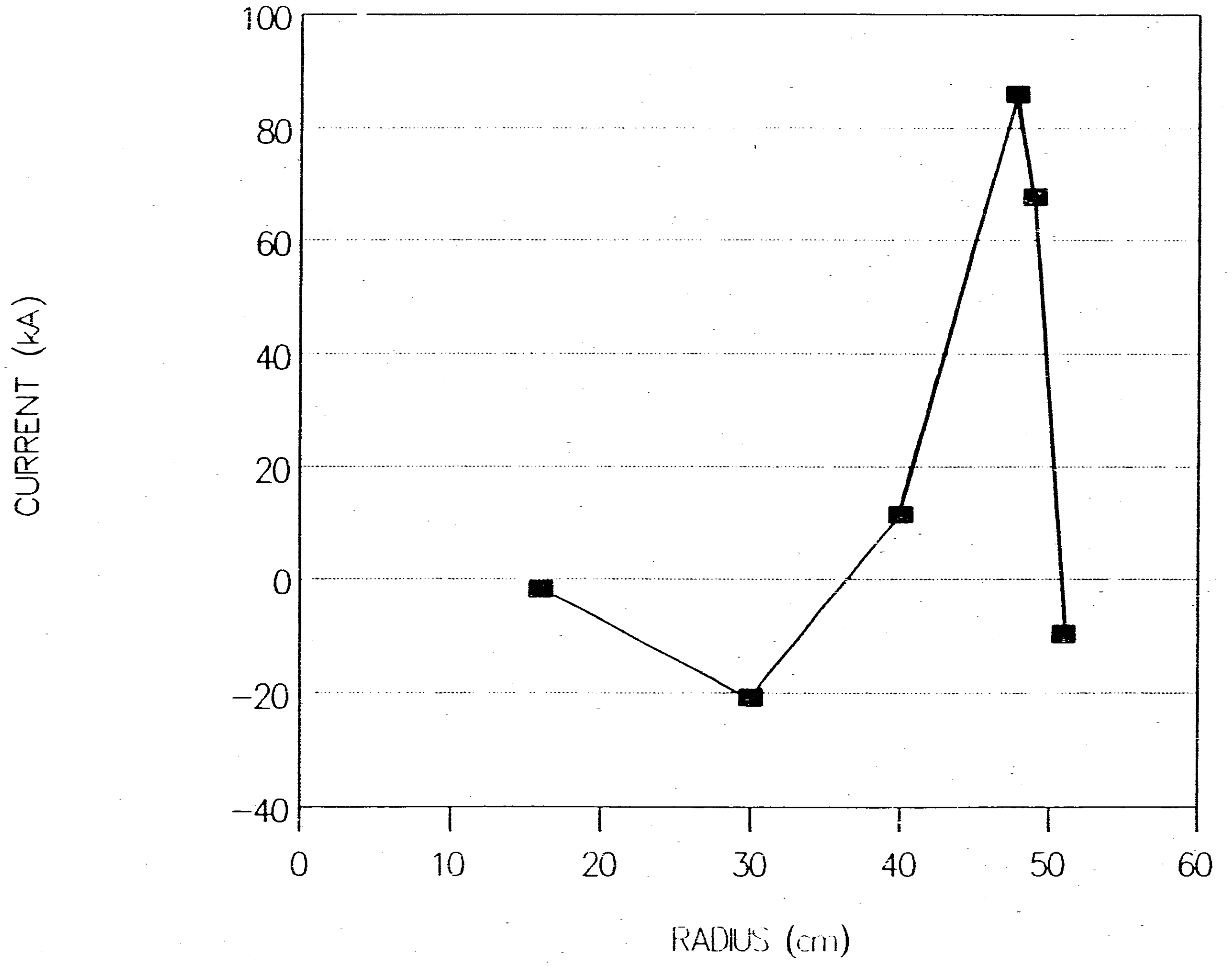

Figure 4. Time averaged current profile for run **AA** near end of run with $I_b = 1.8$ MA.

LLNL PLASMOID PROPAGATION

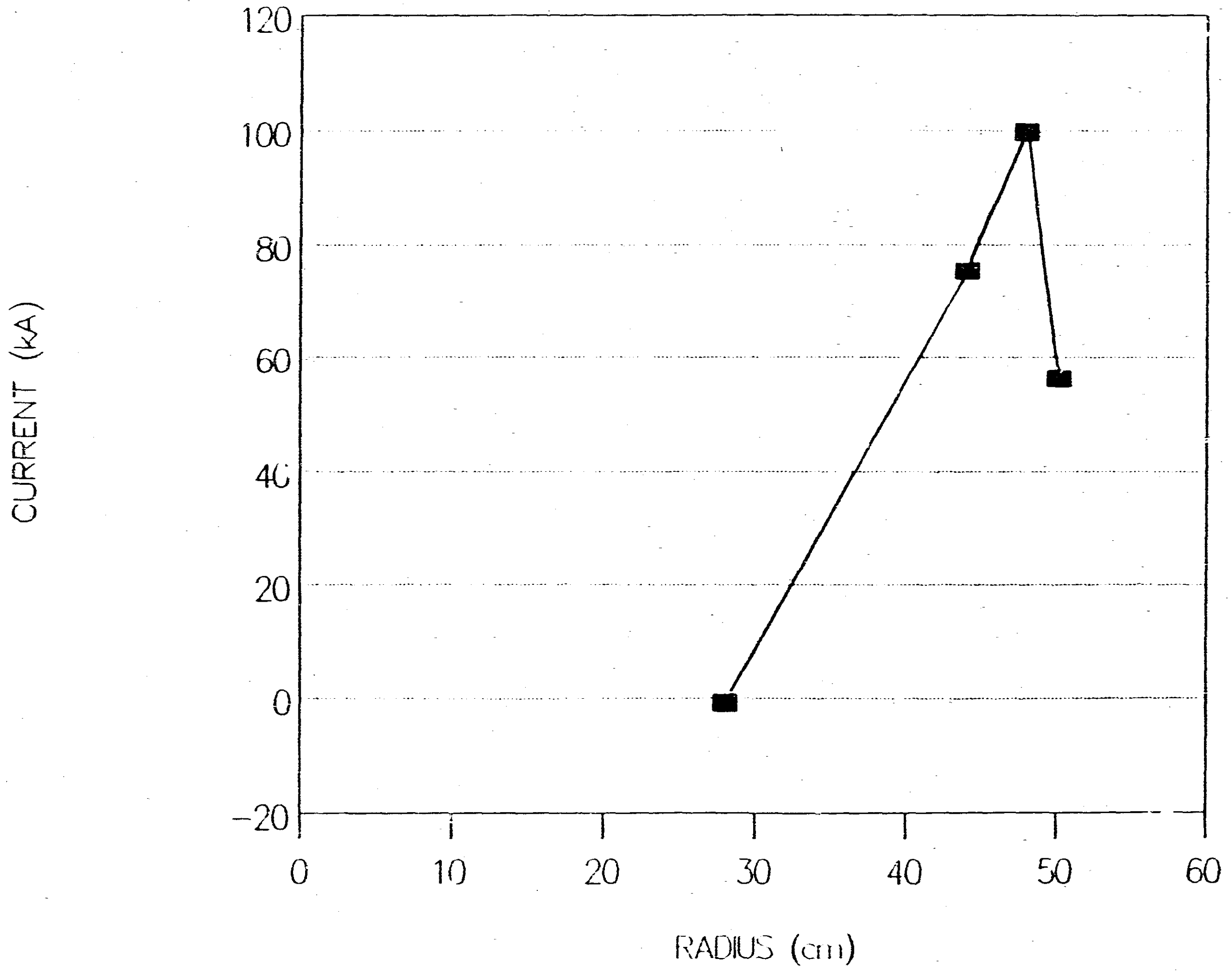

Figure 5. Time averaged current profile for run AB (hollow beam) near end of run with $I_b = 1.8$ MA.

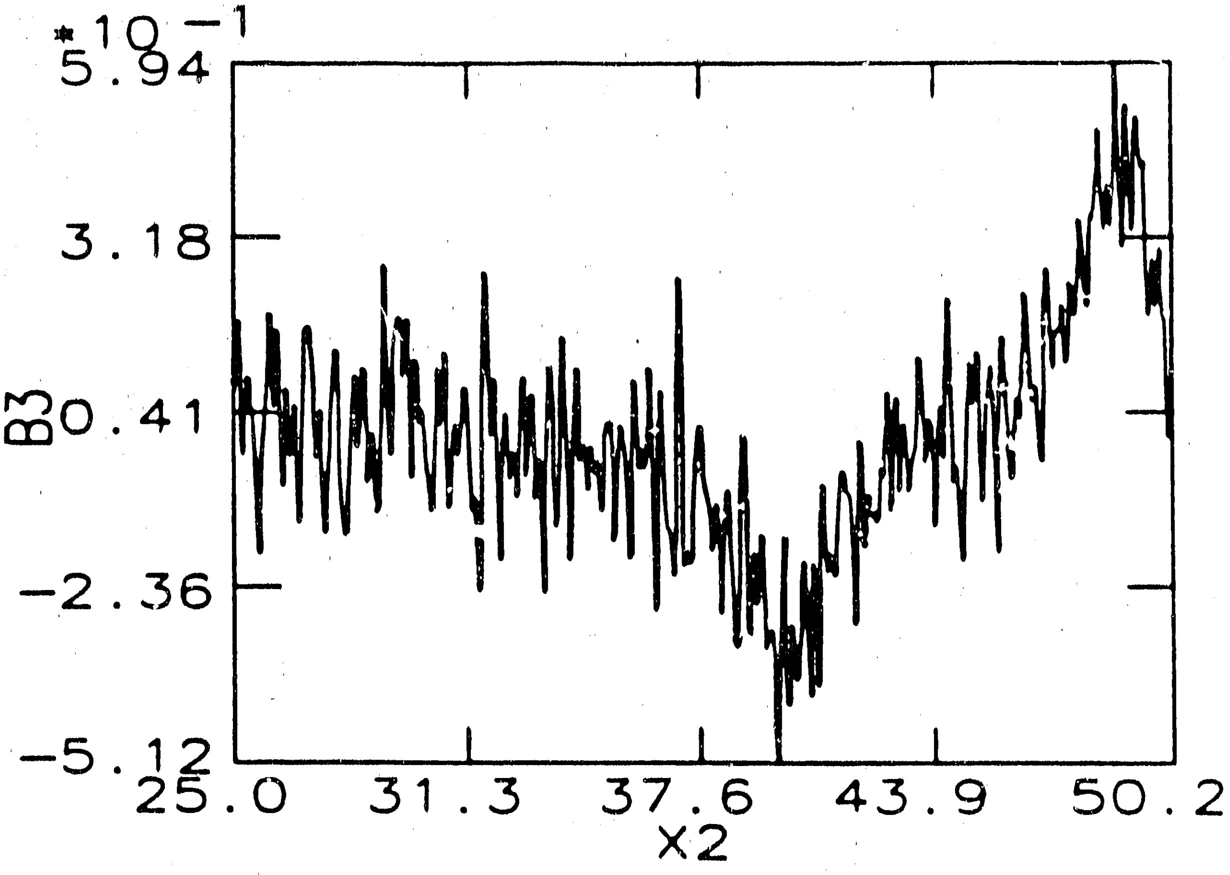

Figure 6. Periodic simulation AC, B_θ (B3, 0.6 kG) versus R (cm) at ct = 500 cm for $I_b = 7.2$ MA.

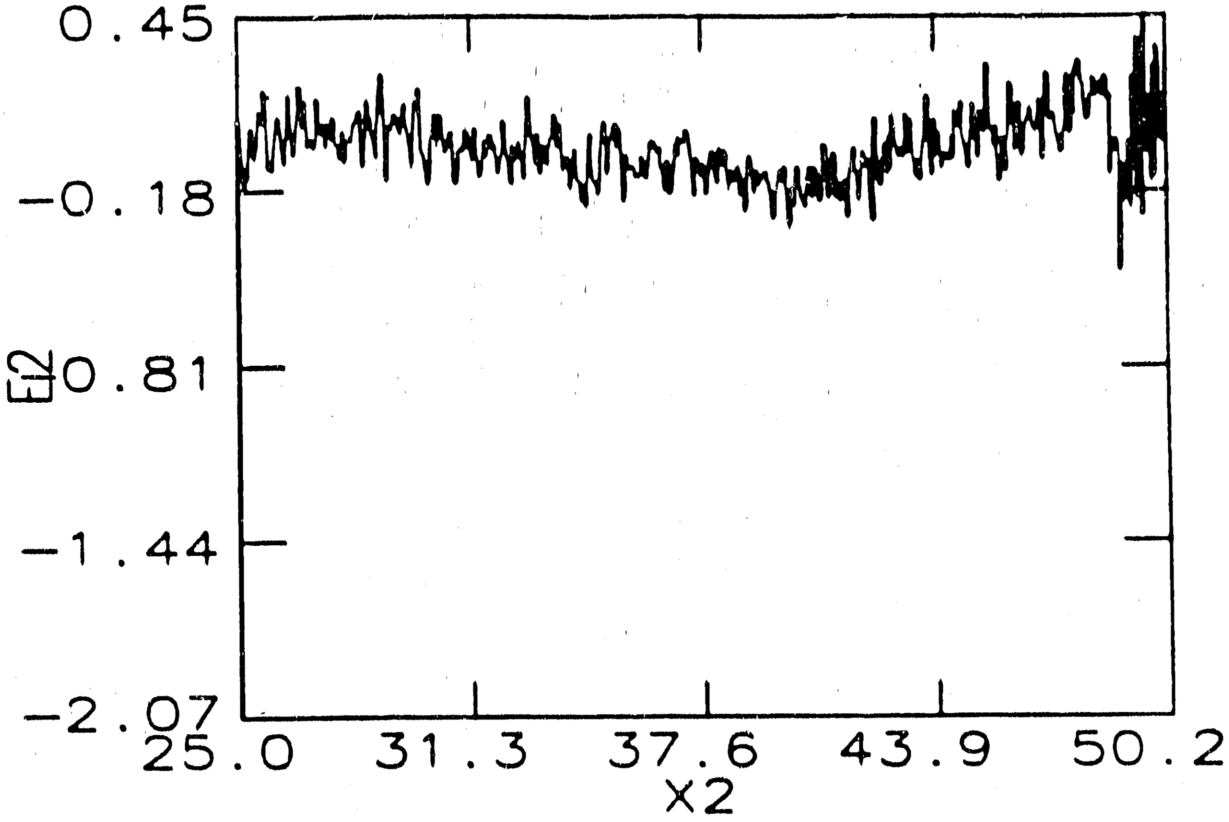

Figure 7. Periodic simulation AC, E_r (E2, 0.51 MeV/cm) versus R (X2, cm) at ct = 500 cm for I_b = 7.2 MA.

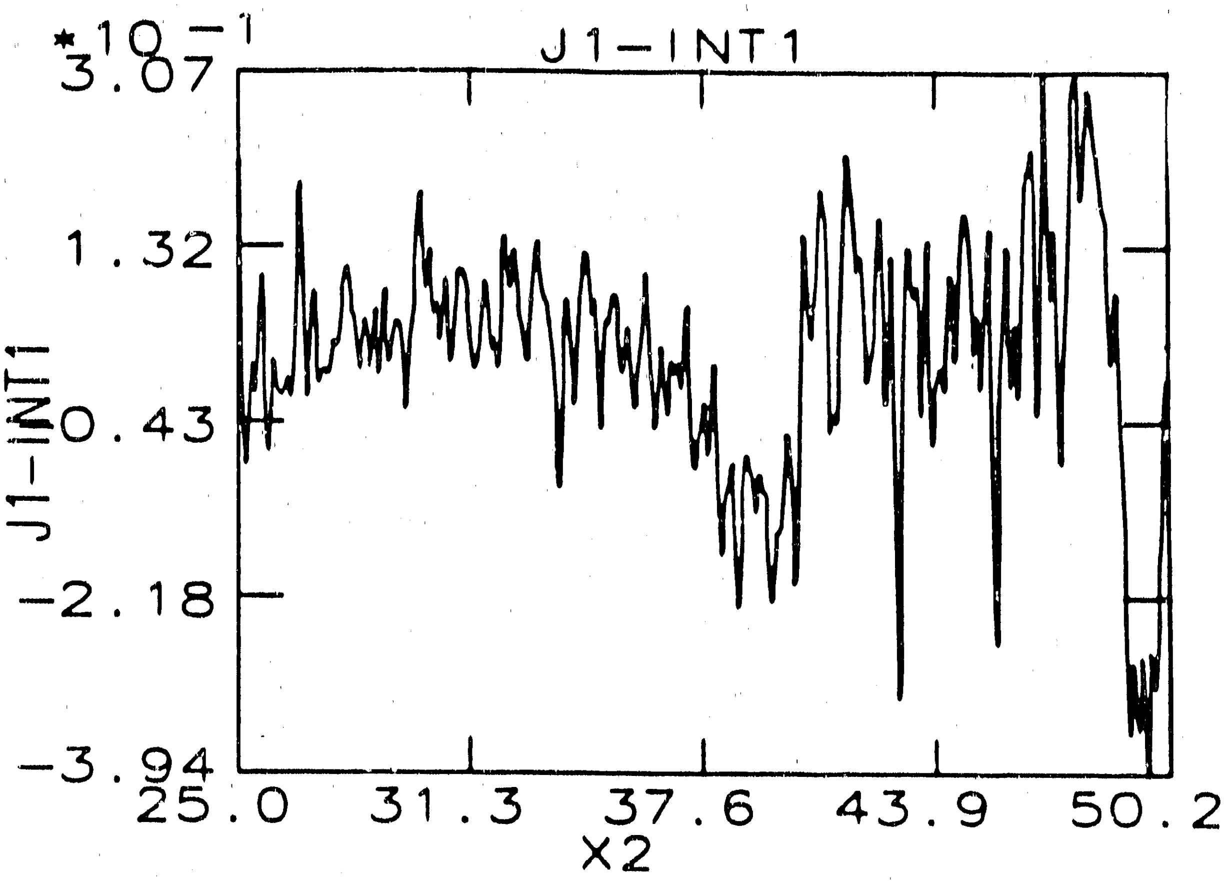

Figure 8. Periodic simulation AC, axially-integrated J_z versus R (X2, cm) at $ct = 500$ cm for $I_b = 7.2$ MA.

LLNL PLASMOID PROPAGATION

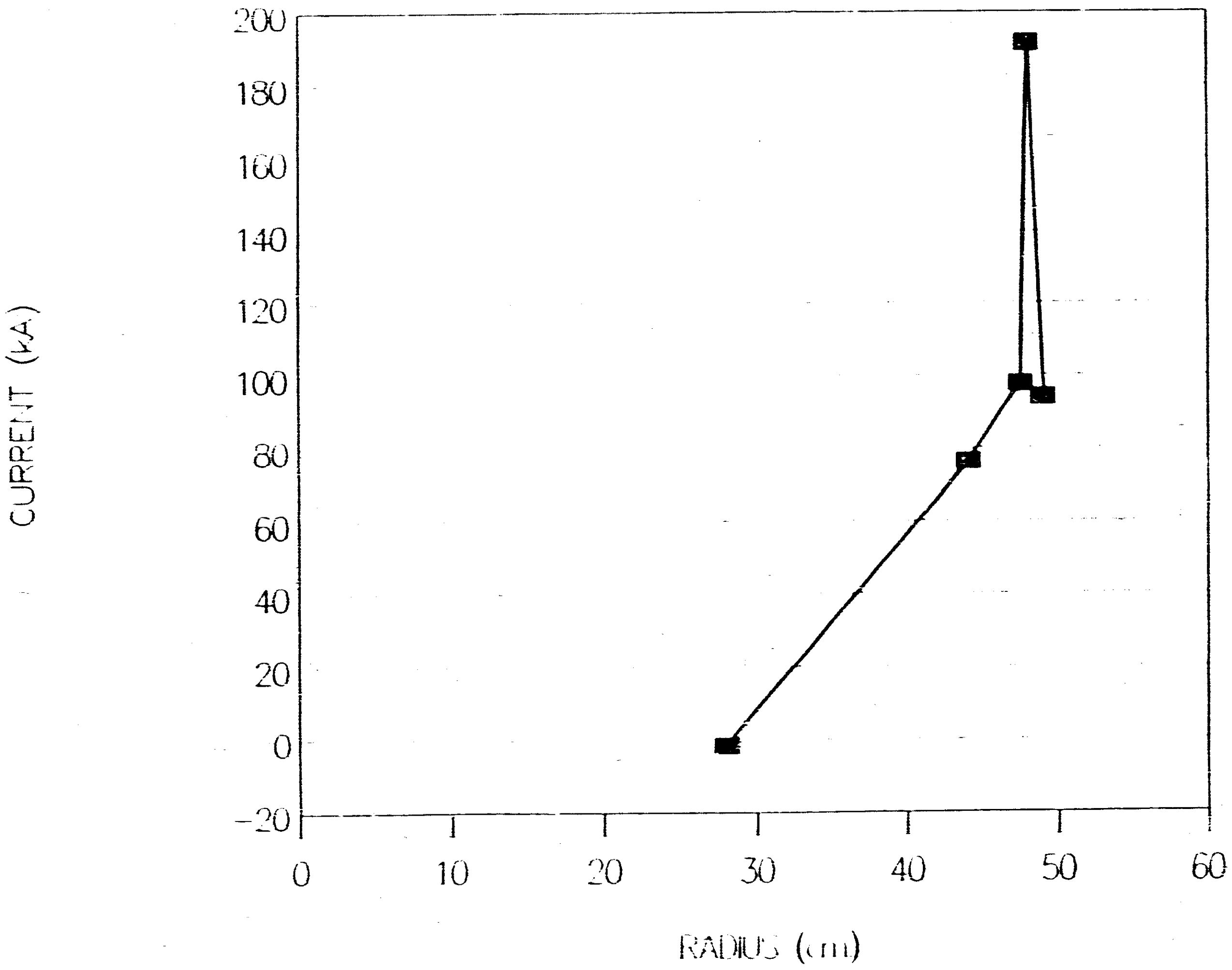

Figure 9. Time averaged current profile for run AC near end of run with $I_b = 7.2$ MA.

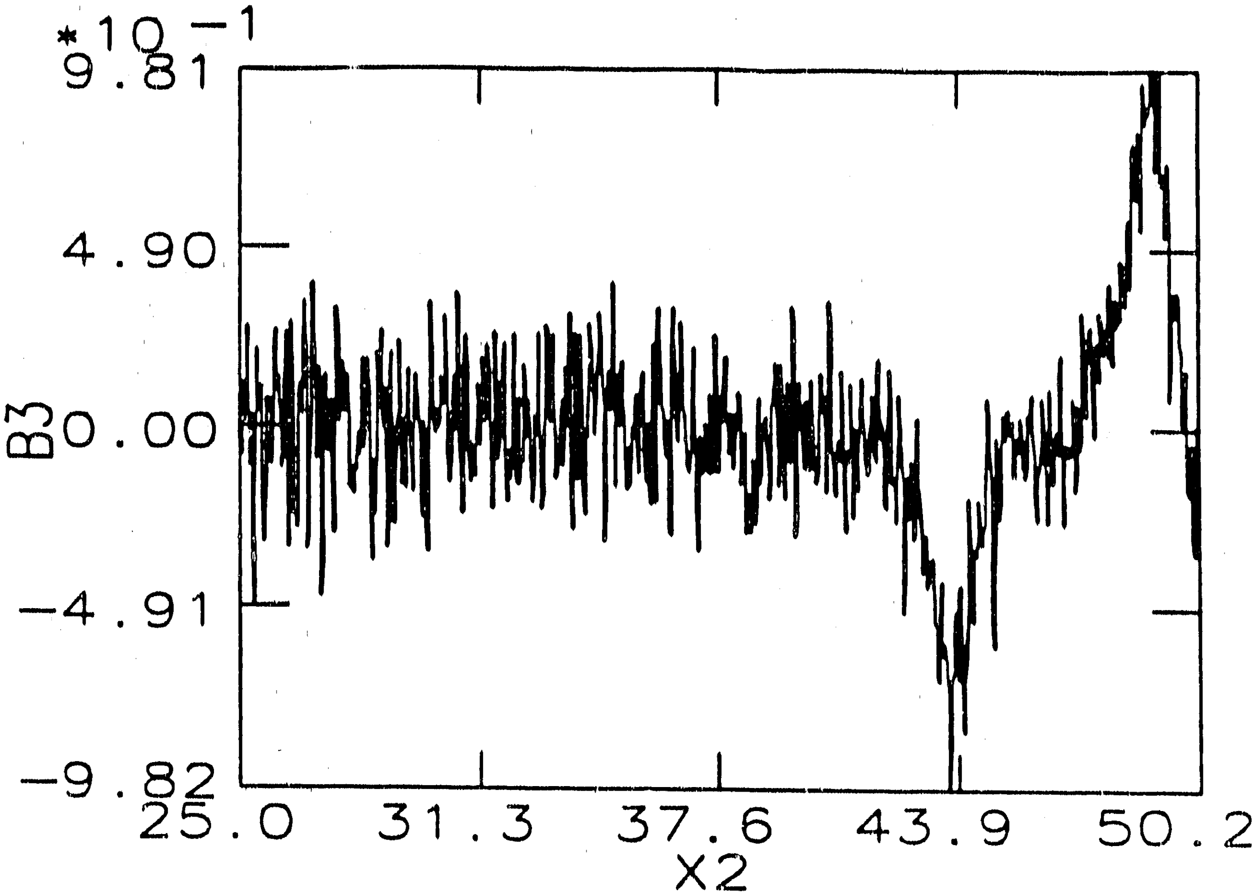

Figure 10. Periodic simulation AD, B_θ (B3, 0.6 kG) versus R (X2, cm) at $ct = 200$ cm for $I_b = 28.8$ MA.

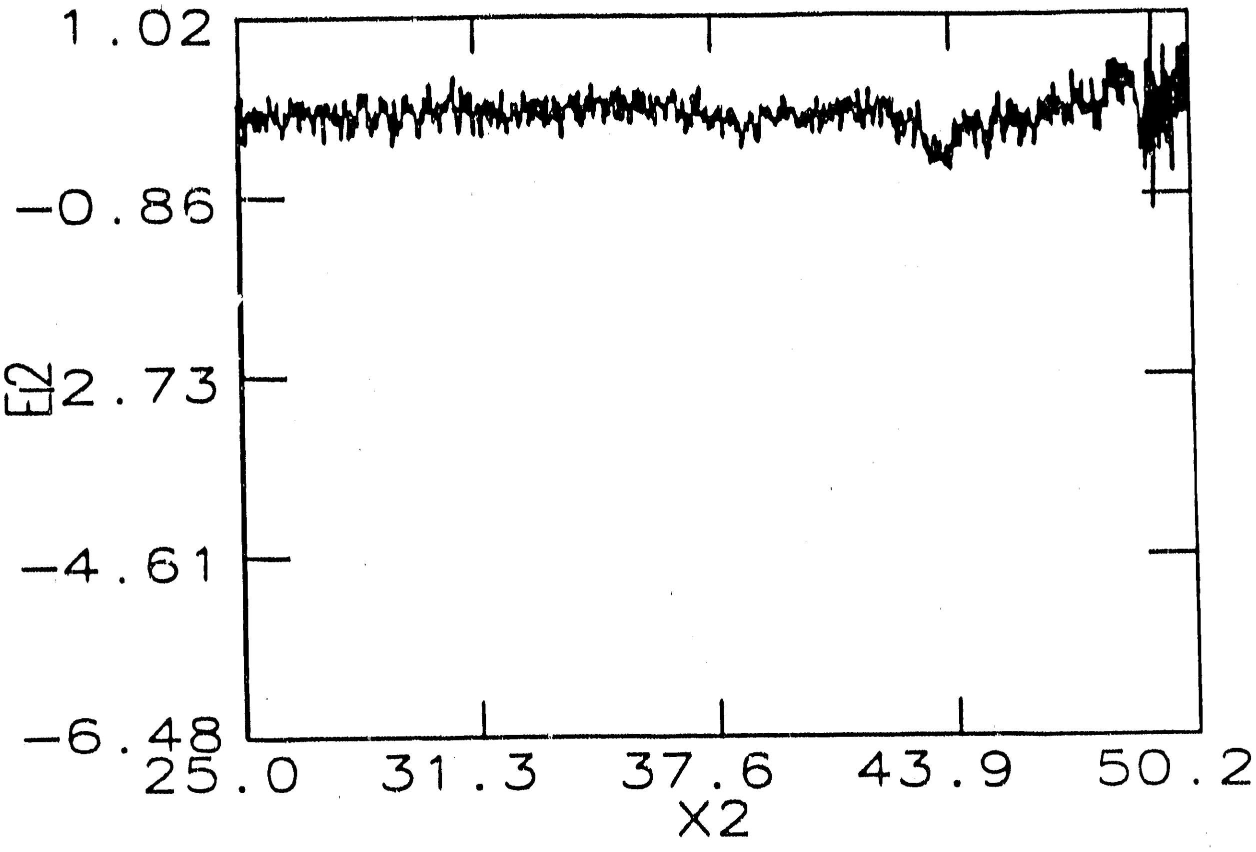

Figure 11. Periodic simulation AD, E_r (E2, 0.51 MeV/cm) versus R (X2, cm) at ct = 200 cm for I_b = 28.8 MA.

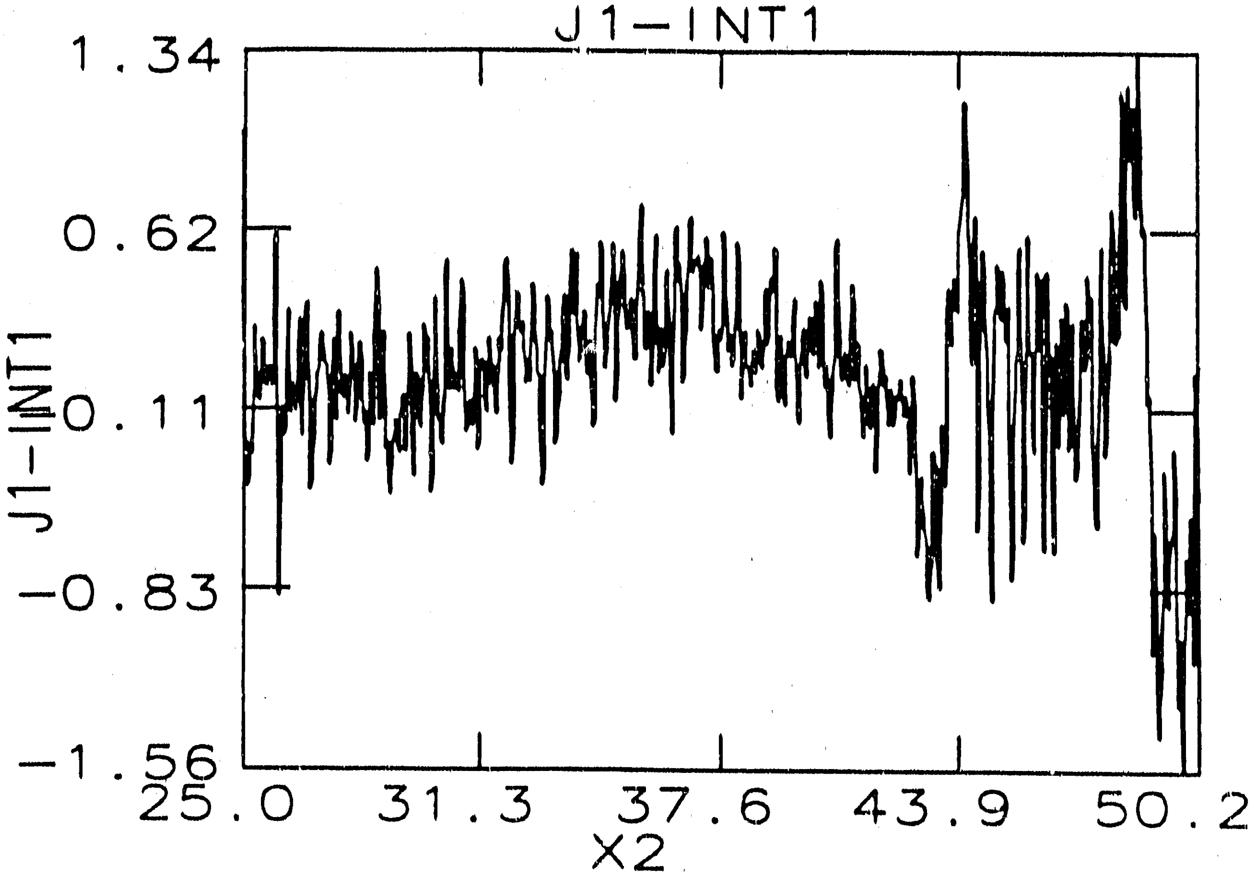

Figure 12. Periodic simulation AD, axially-integrated J_z versus r at $ct = 200$ cm for $I_b = 28.8$ MA.

LLNL PLASMOID PROPAGATION

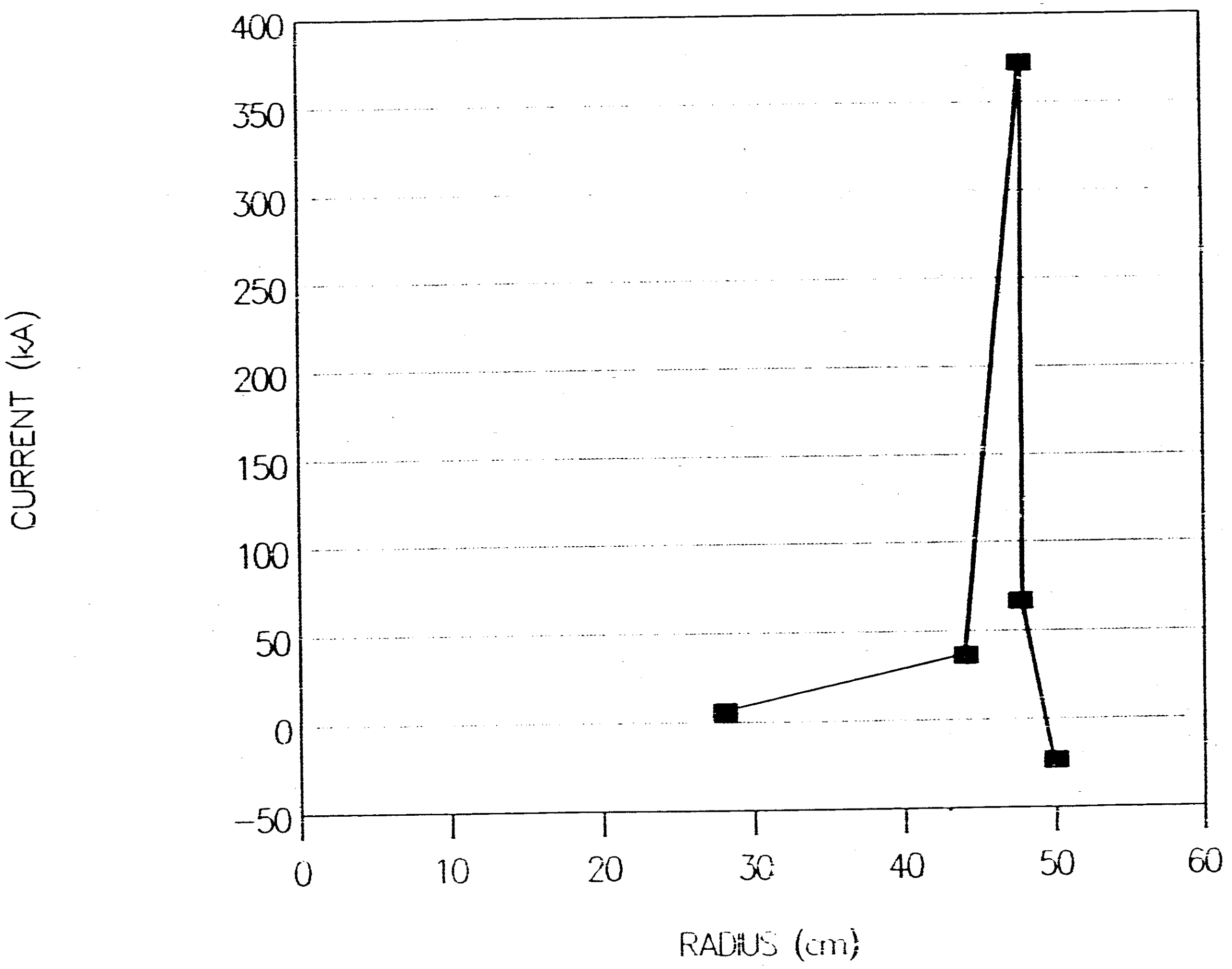

Figure 13. Time averaged current profile for run AD near end of run with $I_b = 28.8$ MA.

LLNL PLASMOID PROPAGATION

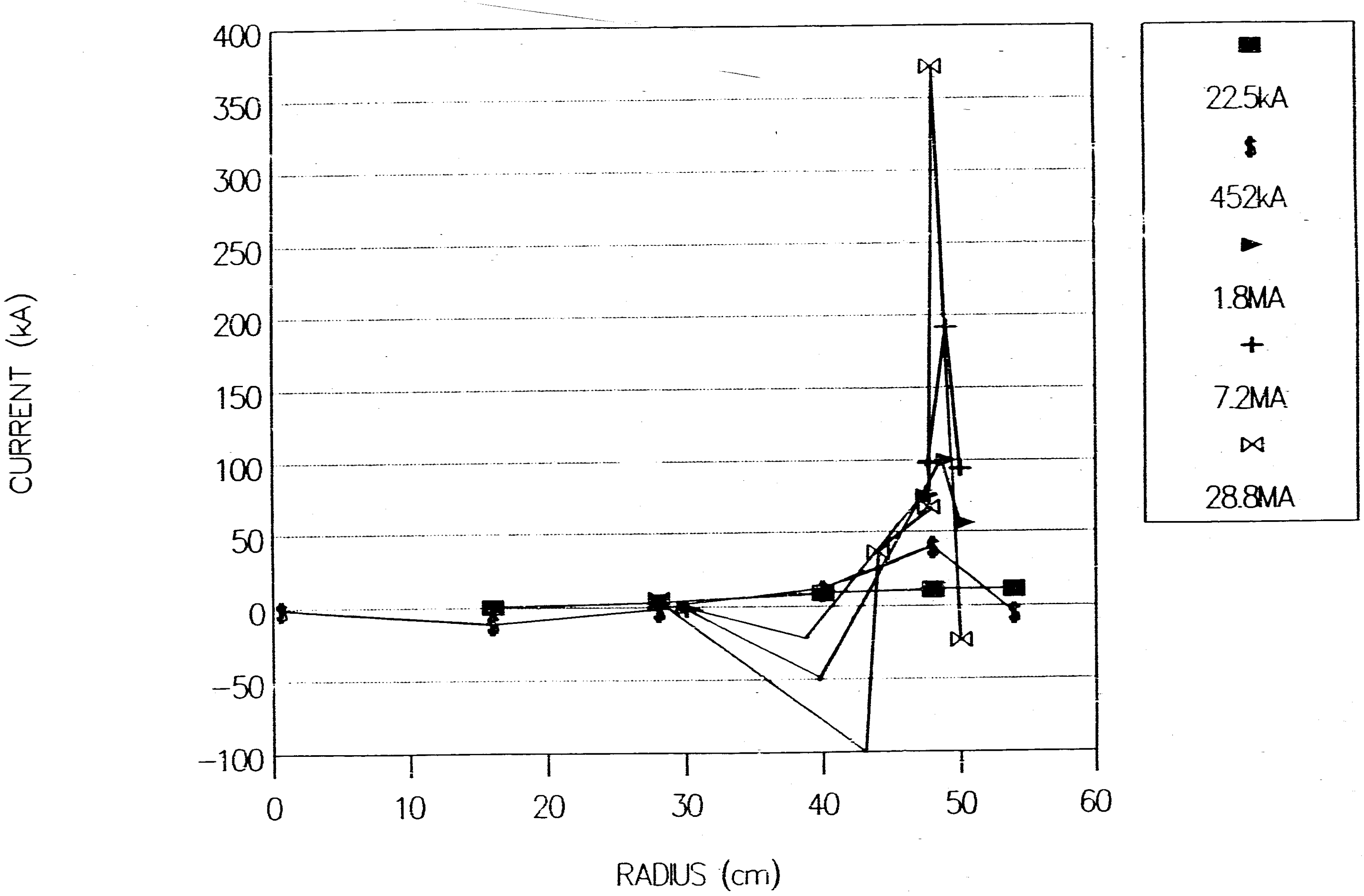

Figure 14. Time averaged current profile comparing different I_b for five runs.

LLNL PLASMOID PROPAGATION

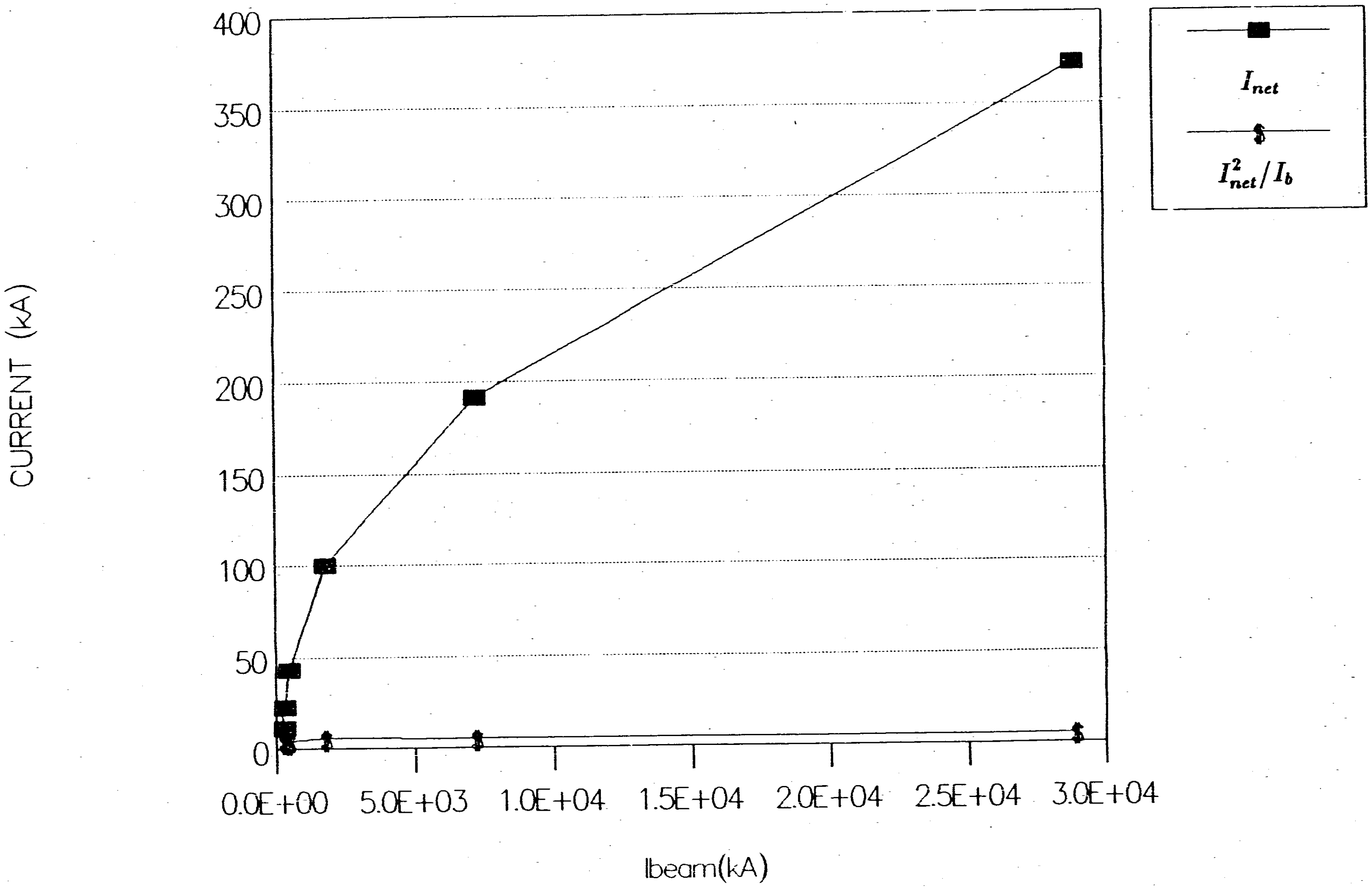

Figure 15. Net current as it scales to the square root of beam current.

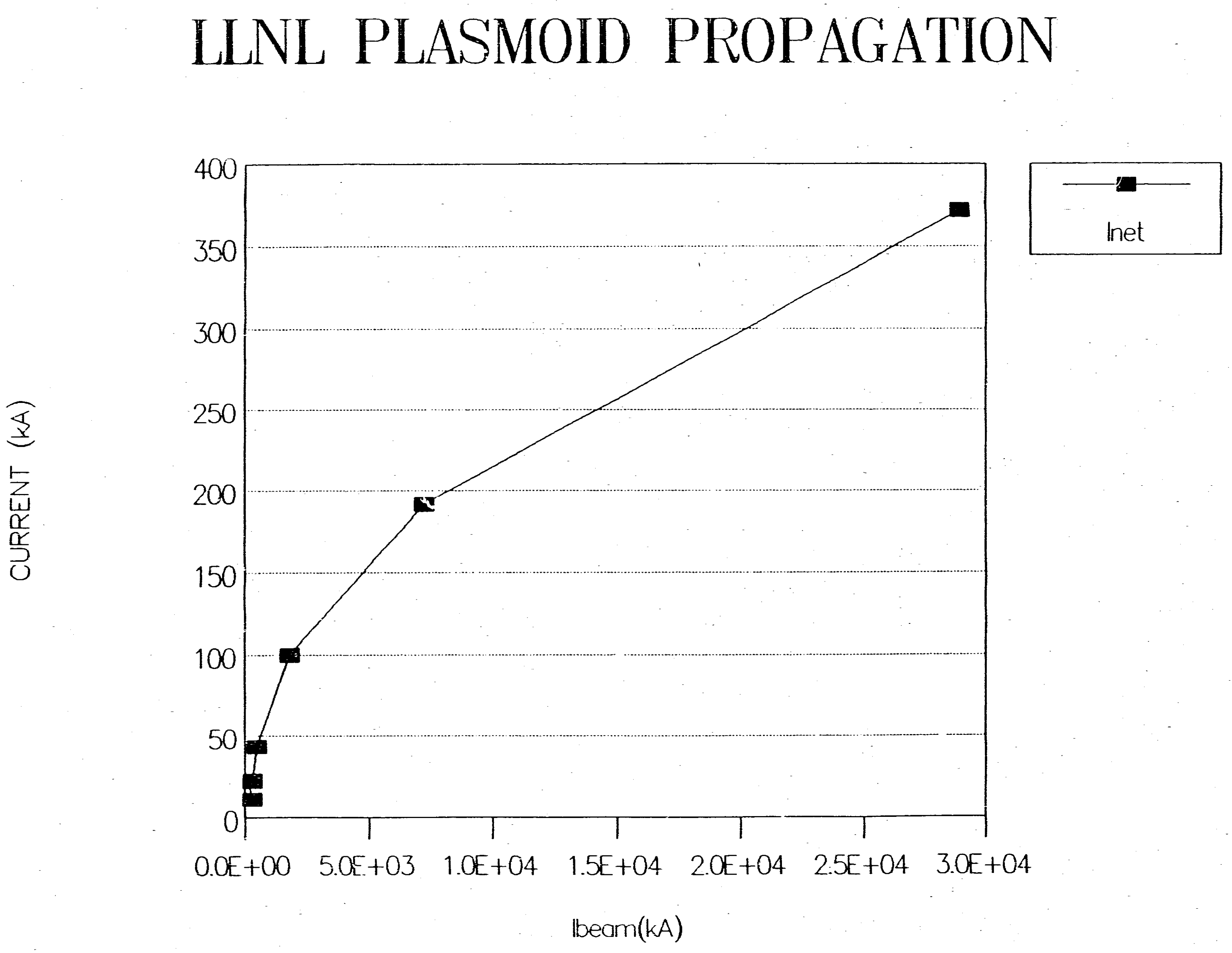

Figure 16. Simulation results showing net current for different beam currents.

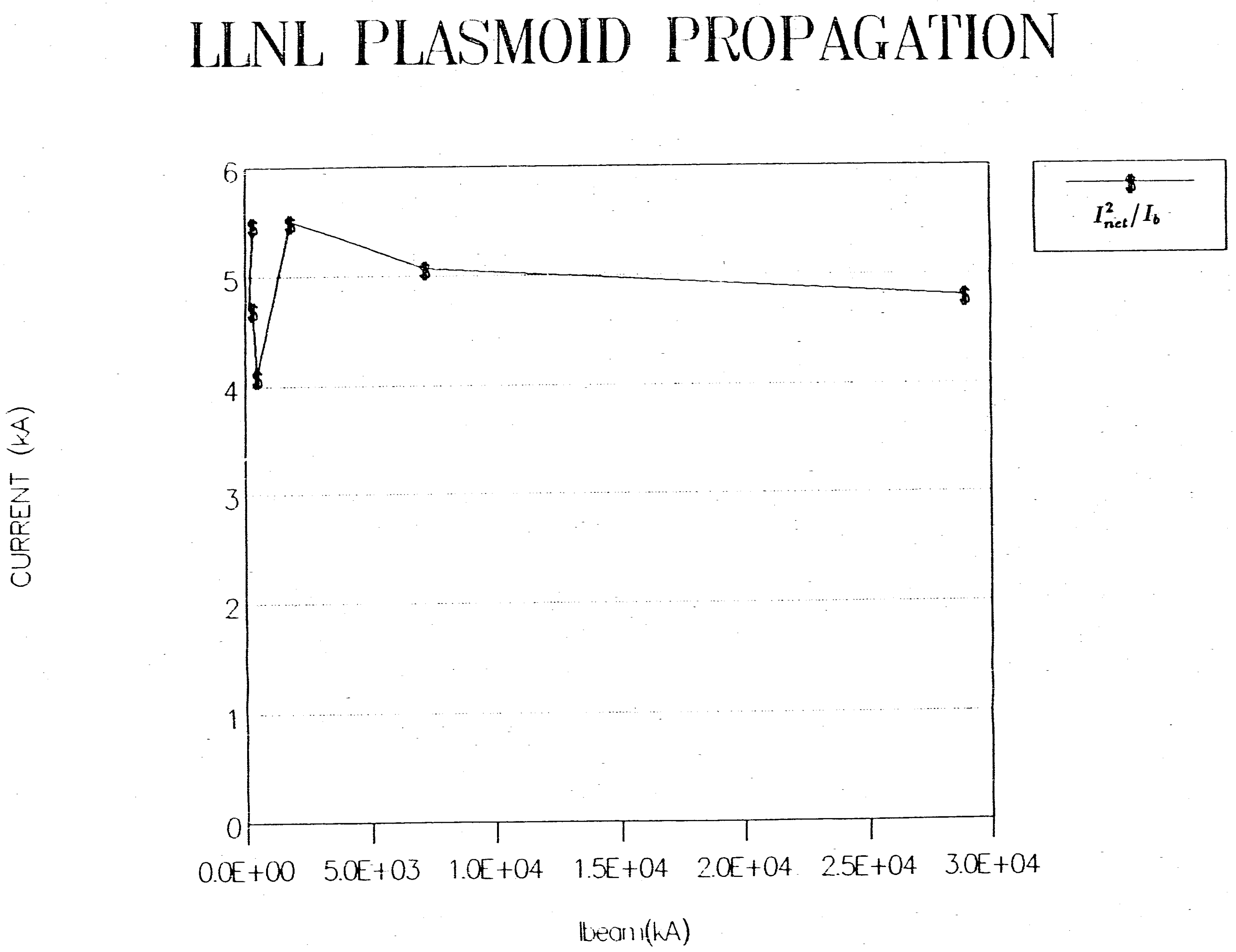

Figure 17. Simulation results showing the square root of the beam current for different beam currents.

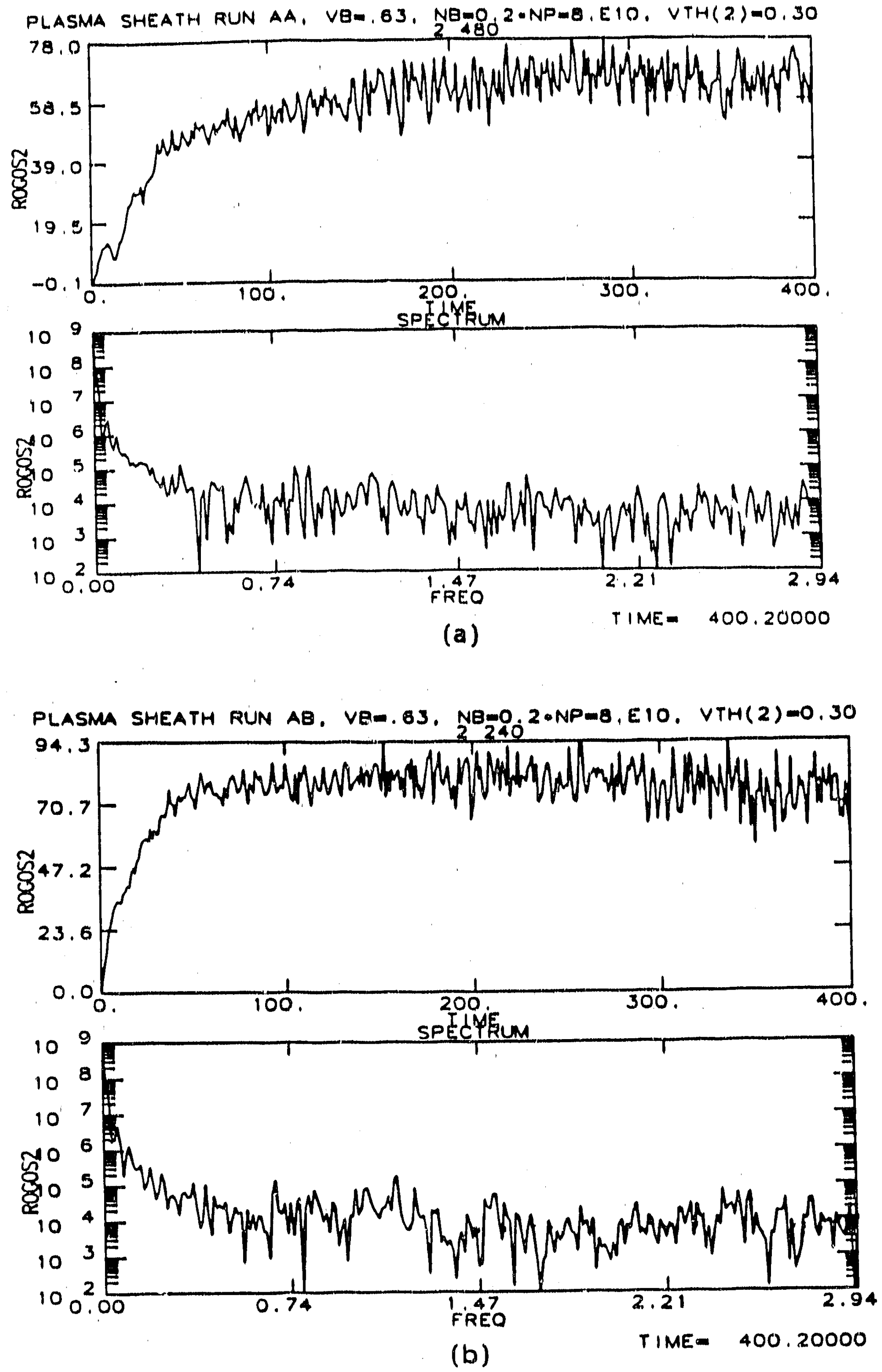

Figure 18. Periodic simulation results comparing time history and frequency spectrum of the net current for two runs. $I_b = 1.8$ MA. Current in units of 1.35 kA, frequency in units of $\omega_0 = 3 \times 10^{10}$ rad/s. (a) run AA, (b) run AB (hollow beam).

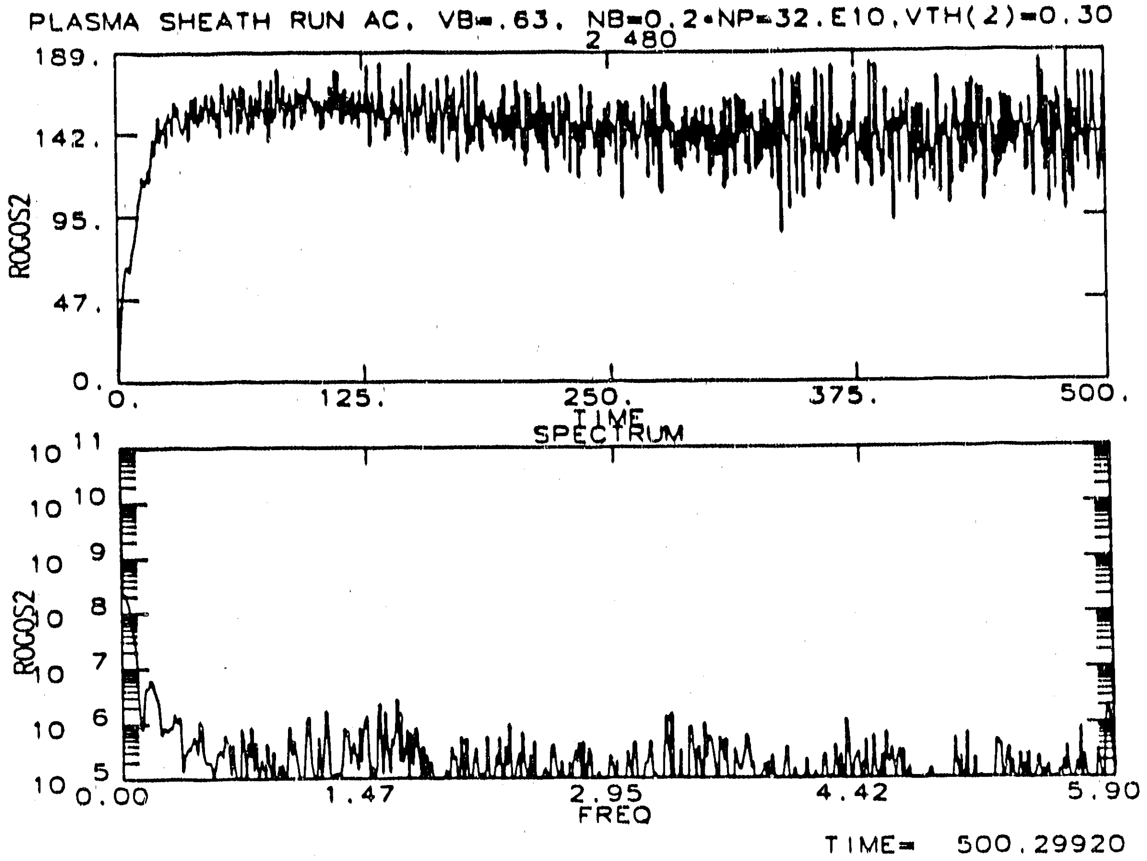

Figure 19. Periodic simulation AC, time history and frequency spectrum of the net current. $I_b = 7.2$ MA. Current in units of 1.35 kA, frequency in units of $\omega_0 = 3 \times 10^{10}$ rad/s.

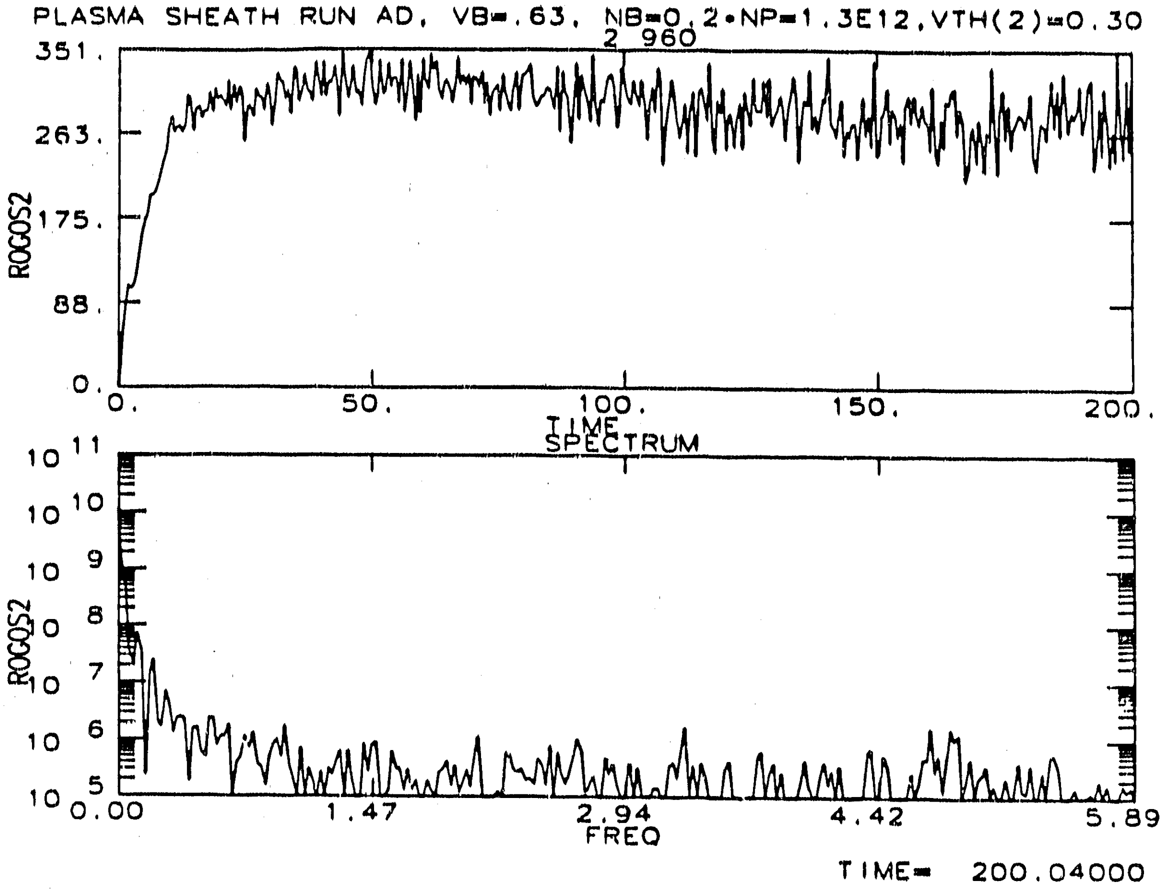

Figure 20. Periodic simulation AD, time history and frequency spectrum of the net current. I_b = 28.8 MA. Current in units of 1.35 kA, frequency in units of $\omega_0 = 3 \times 10^{10}$ rad/s.

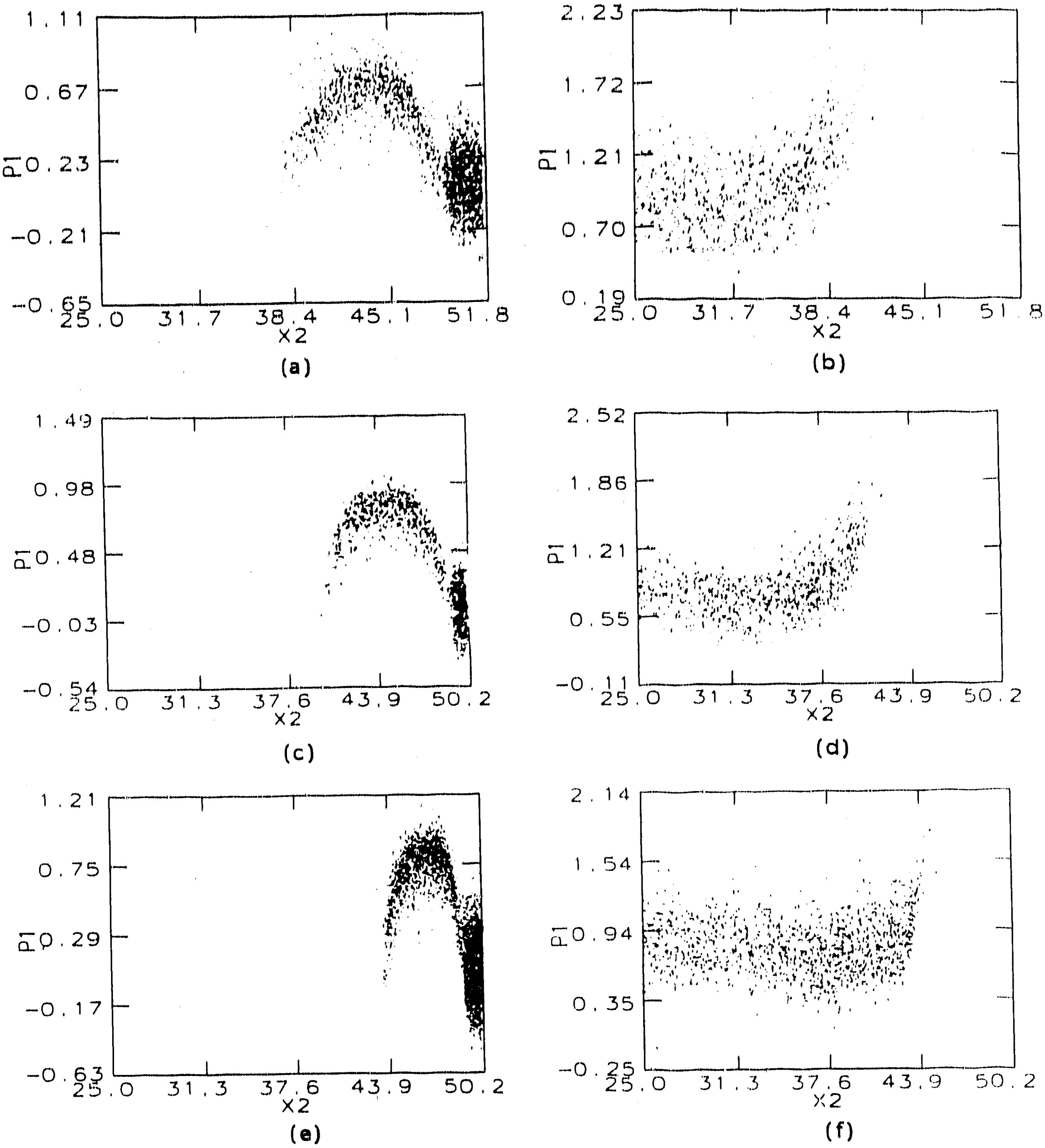

Figure 21. Particle distribution phase-space plot of axial momentum (P1 $\equiv \beta_z\gamma$) versus radial position (X2, cm). Left-hand plot is sheath electrons, right-hand plot is beam electrons. (a) and (b) 1.8 MA run AB at ct = 400 cm. (c) and (d) 7.2 MA run AC at ct = 500 cm. (e) and (f) 28.8 MA run AD at ct = 200 cm.

3.0 LAMINAR FLOW EQUILIBRIUM MODEL

We propose a laminar flow model (similar to a model that has been used for magnetic insulation calculations[2]) as a first simple description of the electron equilibrium in the plasmoid. By "laminar" we mean that $v_r = 0$. Nevertheless, we assume that all electrons now in the plasmoid of radius r_b were born at zero energy on a zero-potential ($\phi = 0$) surface coinciding with a conducting pipe at radius $R_w \geq r_b$. Energy conservation then gives the usual relativistic factor

$$\gamma - 1 = e\phi/mc^2 \tag{1}$$

where e (> 0) and m are the electron charge and mass. The ion-beam density n_i and the axial velocity v_{zi} are assumed to be free parameters independent of radius for $r < r_b$ and $v_{zi} = 0$ for $r > r_b$. Conservation of axial canonical momentum for the plasmoid electrons gives

$$P_z \equiv \gamma m v_z - eA_z = 0 \tag{2}$$

where we have taken the vector potential $A_z = 0$ at the $\phi = 0$ surface.

The radial electric field is defined in terms of the potential by

$$E_r = -\frac{d\phi}{dr} = -\frac{mc^2}{e}\frac{d\gamma}{dr} \tag{3}$$

and is given in terms of the plasma sources by Poisson's equation

$$\frac{1}{r}\frac{d}{dr}\left(r\frac{d\phi}{dr}\right) = \frac{e\,(n_e - n_i)}{\epsilon_0} \quad . \tag{4}$$

Thus, using Eqs. 3 and 4 the electron density is

$$n_e = \frac{\epsilon_0 mc^2}{e^2}\frac{1}{r}\frac{d}{dr}\left(r\frac{d\gamma}{dr}\right) + n_i \quad . \tag{5}$$

The azimuthal magnetic field is defined in terms of the vector potential from Eq. 2 by

$$B_\theta = -\frac{d}{dr}A_z = -\frac{m}{e}\frac{d}{dr}(\gamma v_z) \quad . \tag{6}$$

Combined with E_r from Eq. 3 this gives the radial force-balance equation $E_r - v_z B_\theta = 0$, which gives $E_r \approx cB_\theta$ in agreement with the ISIS simulation results. Ampere's law relates B_θ to the plasma sources by

$$\frac{1}{r}\frac{d}{dr}(rB_\theta) = \mu_0 e\left(n_i v_{zi} - n_e v_z\right) \quad . \tag{7}$$

Substituting B_θ from Eq. 6 into Eq. 7 gives

$$\frac{1}{r}\frac{d}{dr}\left[r\frac{d}{dr}(\gamma v_z)\right] + \frac{\mu_0 e^2}{m}\left(n_i v_{zi} - n_e v_z\right) = 0 \quad . \tag{8}$$

Substituting the electron density n_e from Eq. 5 into Eq. 8 gives a second-order radial nonlinear differential equation for the electron velocity v_z:

$$\frac{1}{r}\frac{d}{dr}\left(\gamma^2 r\frac{dv_z}{dr}\right) = \frac{\omega_b^2}{c^2}\gamma\left(v_z - v_{zi}\right) \quad . \tag{9}$$

For simplicity we analyze the nonrelativistic limit $\gamma \approx 1$, valid for $v_z \ll c$, which linearizes the equation. We also ignore cylindrical effects, valid for $r\omega_b/c \gg 1$. Defining $y \equiv v_z - v_{zi}$ and $x \equiv (r - r_b)\omega_b/c$, Eq. 9 reduces to

$$\frac{d^2y}{dx^2} = y \qquad (x < 0) \tag{10}$$

which has the general solution $y = c_1 e^{x} + c_2 e^{-x}$. To keep y finite for large negative x ($r \ll r_b$), we require $c_2 = 0$. Outside the beam, $v_{zi} = 0$ and n_i may be different than inside the beam. Defining $\lambda^2 \equiv n_i(r > r_b)/n_i(r < r_b)$, the electron velocity is

$$\frac{d^2v_z}{dx^2} = \lambda^2 v_z \qquad (x > 0) \tag{11}$$

which has the general solution $v_z = c_3 e^{\lambda x} + c_4 e^{-\lambda x}$. We assume $(r_w - r_b)\lambda\omega_b/c \gg 1$ (many plasma skin depths between beam and wall). To keep v_z finite for large positive x, we require $c_3 = 0$. Thus, the velocity is described by

$$v_z = \begin{cases} v_{zi} + c_1 e^{x} & (x < 0) \\ c_4 e^{-\lambda x} & (x > 0) \end{cases} \tag{12}$$

Because the potential ϕ and its derivative, the electric field, must be continuous at the beam edge $x = 0$, this defines the two constants and gives

$$\frac{v_z}{v_{zi}} = \begin{cases} 1 - \dfrac{\lambda}{1+\lambda} e^{x} & (x < 0, r < r_b) \\ \dfrac{1}{1+\lambda} e^{-\lambda x} & (x > 0, r > r_b) \end{cases} \tag{13}$$

Thus, at the $x = 0$ $(r = r_b)$ the velocity is

$$\frac{v_z\left(r = r_b\right)}{v_{zi}} = \frac{1}{1+\lambda} \tag{14}$$

which is small if $\lambda \gg 1$, while $v_z \to v_{zi}$ for $\lambda \to 0$.

Several relationships follow from this analysis. From Eq. 6, the magnetic field at the beam edge is

$$B_\theta\left(r = r_b\right) = \frac{m}{e}\frac{v_{zi}}{c}\frac{\lambda}{1+\lambda}\omega_b \tag{15}$$

which vanishes for $\lambda \to 0$ and approaches a constant for $\lambda \gg 1$. The net current in the beam is

$$I_{net}\left(r = r_b\right) = \frac{2\pi r_b}{\mu_0} B_\theta\left(r = r_b\right) = \frac{1}{2} I_A \beta_{zi} \frac{\lambda}{1+\lambda}\left(r_b \omega_b / c\right) \tag{16}$$

where $I_A \equiv 4\pi mc/e\mu_0 = 17$ kA. Using the relation

$$\frac{r_b\omega_b}{c} = 2\sqrt{\frac{I_b}{I_A\beta_{zi}}} \qquad (17)$$

where I_b is the ion beam current, Eq. 16 reduces to

$$\frac{I_{net}^2(r_b)}{I_b} = I_A\beta_{zi}\left(\frac{\lambda}{1+\lambda}\right)^2 \quad . \qquad (18)$$

The azimuthal magnetic field exerts a confining pressure $B_\theta^2(r_b)/2\mu_0$ on the ion beam which must be countered in equilibrium by a finite ion-beam pressure $P_i = n_iT_i$. Using Eq. 13 and equating these two pressures, the ion beam density cancels from the equation, leaving only an expression for the ion temperature

$$T_i = \frac{1}{2}mc^2\beta_{zi}^2\left(\frac{\lambda}{1+\lambda}\right)^2 \quad . \qquad (19)$$

This implies that the ion beam is generally quite hot in equilibrium with $(v_i)_{th}/v_{zi} = \lambda/(1+\lambda)$.

These theoretical predictions are specific and in some cases can be compared with existing ISIS simulations. The square of the net current I_{net}, divided by the beam current I_b, is plotted versus I_b for the simulation results in Fig. 17, and the result is indeed constant at approximately 5 kA independent of beam current. For all of our plasmoid simulations (here and in Ref. 1), we used an ion drift velocity of $\beta_{zi} = 0.62$. For all but the earliest simulations in Ref. 1, we use a plasma density between the wall and beam equal to five times the beam density, or $\lambda = \sqrt{5}$. Therefore, Eq. 18 gives a predicted value of 5.03 kA for the constant of proportionality between $I_{net}^2(r_b)$ and I_b. Moreover, Eq. 19 gives a predicted ion-beam temperature for equilibrium of $T_i = 46.9$ kV. In the ISIS simulations in Ref. 1, we varied T_i and empirically found that 43 kV gave a good equilibrium for beam currents of 22.5 kA, 112.5 kA, and 452 kA. In our present research reported here, this same value of 43 kV was used for the ion-beam temperature in all of the simulations and no noticeable contraction or expansion of the ion beam was observed. These two agreements are excellent, particularly when the wide range of beam currents $I_b = 22.5$ kA–28.8 MA is considered.

The radial profile of the electron axial velocity in Eq. 13 also can be compared with simulation. In all of the MRC ISIS simulations, λ was large (usually $\lambda^2 = 5$). The description of the electron velocity v_z in Eq. 13 is consistent with the simulation results in that v_z/v_{zi} was small at the beam edge $x = 0$ and increased rapidly over a few beam skin depths c/ω_b until $v_z \approx v_{zi}$ in the beam interior. The near equality of E_r and cB_θ in the simulations also is consistent with the laminar flow model used here.

Several scaling predictions remain to be verified. One trend apparent from Eq. 13, but not yet verified by computer simulation, is that v_z at the beam edge increases as λ decreases and $v_z(r = r_b) \rightarrow v_{zi}$ as $\lambda \rightarrow 0$. From Eq. 15, the magnetic field at the beam edge is proportional to λ for $\lambda \ll 1$, and saturates at a constant for $\lambda \gg 1$. The constant of proportionality I_0 between $I^2_{net}(r_b)$ and I_b,

$$I_0 \equiv I_A \beta_{zi} \left(\frac{\lambda}{1+\lambda} \right)^2 \quad , \tag{20}$$

is linearly proportional to the ion beam axial velocity β_{zi} which was never varied from 0.62 in our series of simulations. There is also a strong dependence of I_0 on λ. For $\lambda \ll 1$, I_0 is proportional to λ^2—that is, to the ratio of exterior plasma density to beam density. Combined with Eq. 18, this predicts $I_{net}(r_b) \propto r_b\sqrt{n_i(r > r_b)}$, or to the number of *exterior plasma* skin depths across the beam. For $\lambda \gg 1$, as in the simulations, $I_{net}(r_b) \propto r_b\sqrt{n_b}$, or to the number of *beam* skin depths across the beam. The ion-beam temperature for equilibrium is extremely sensitive to parameters. It is proportional to β^2_{zi} and, for $\lambda \ll 1$, to λ^2. For $\lambda \gg 1$, it saturates at $(T_i)_{max} = 1/2\ mv^2_{zi}$. These changes in scaling should be verified by simulation.

4.0 CONCLUSIONS

Increasing the beam current to 28.8 MA does not appear to strongly affect the equilibrium scaling discussed in our earlier reports. While there is some indication that the current sheath thickness is now not decreasing as rapidly at higher beam current as at lower values, the net current still scales as $I_{net} \sim I_{beam}^{1/2}$. The beam temperature required for equilibrium appears to remain constant at 43 kV independent of beam current.

To try to shed light on the observed scalings in the ISIS code results, we completed a laminar flow model of the electrons. Specific predictions were obtained for radial profiles as well as for the net current and the ion-beam temperature necessary for equilibrium. In all cases, the predictions agreed very well with the ISIS simulations, and new parameter scalings were brought out which should be verified.

5.0 FUTURE WORK

There are many beam and background plasma parameters that affect the plasmoid equilibrium. In spite of having carried out extensive and complex simulations over the last two years, some of these parameters have remained fixed. The laminar flow model presented here indicates several interesting parameter scalings that, if verified, would further our confidence in this model. We could continue simulations on to higher currents, but we believe that this scaling is adequately verified over the present range of I_b = 22.5 kA–28.8 MA. For instance, by moving the metal "core" boundary to larger radius (i.e., R = 32 cm) and limiting the plasma sheath thickness to four Debye lengths we could probably run a 115 MA case to t = 100 (3.3 ns) in about 15 CPU hours, but we expect little new information to result. A set of 7 MA cases allowing variation in beam ion temperature and velocity, sheath electron temperature, and sheath thickness and density would indicate how sensitive the high-current equilibrium is to these parameters and would further test the laminar flow model in new areas.

If an analytic model can be found that adequately predicts the wavelength of the fastest growing two-stream-like instability we should be able to resolve one wavelength in the axial direction sufficiently to determine a growth rate at moderately high (~ 2 MA) current. This would provide a useful data point in the regime where the "mixing" region thickness is much less than the beam radius and whether or not it stays that way with the instability present.

REFERENCES

1. M. A. Mostrom and M. M. Campbell, "Equilibrium and Microstability of Plasmoid Propagation," MRC/ABQ-R-1026, Mission Research Corporation, Albuquerque, NM, May 1988.

2. M. A. Mostrom, M. E. Jones and L. E. Thode, "Magnetically Insulated Plasma Sheath in Coaxial Transmission lines with an External Magnetic Field," *J. Appl. Phys.* 52 (3), March 1981.

APPENDIX A

LOW-MODERATE BEAM-CURRENT SIMULATION RESULTS AT AFWL

Following is an excerpt from the quarterly progress report for September 1988–April 1989.

A.i SIMULATION RESULTS

To reduce computation time (by a factor of ~ 40) we have used a "nearly 1-D" model to generate equilibria. Cases for plasmoid propagation with ion currents ranging from 22 kA to 1.8 MA have been run thus far. This corresponds to the number of skin depths across the beam, $\omega_{be} r_b / c$, in the range 2.9 to 26.0, respectively. During the course of simulating higher currents, we noted that noise levels in the diagnostics increased with the current to a point that made interpretation very difficult by 1.8 MA. Increasing the current further to > 7 MA would produce nearly unreadable results. We, therefore, decided to try reducing the noise to acceptable levels. A series of runs (on the AFWL CRAY) were done changing the number of grid points, the "current smoothing" and/or the number of particles-per-cell in the axial direction (X1, the dimension that is being approximately eliminated) and in the radial direction (X2). Most of these tests were done at 22 kA where the run time was short but the noise level still easily observable. The "current smoothing" namelist parameters for X1 and X2 (NSM1, NSM2) and the number of particles-per-cell were adjusted separately or concurrently. We conclude that having much more than 10 particles per cell and extensive smoothing with NSM1 = 1, NSM2 = 3 reduced the noise considerably with only two cells (three grid points) in X1. This set of parameters increased the running time by about a factor of two to four over the original case, which still extrapolates to a run time for a 7 MA case of about 8 hours, a high but acceptable cost. We then set up a run at a current of 7.2 MA which had run on the AFWL CRAY to about one-fourth of the equilibration time when the "free" SDI computer charge account was shut down due to lack of funds. Results at that point were not close enough to equilibrium to provide meaningful values. (Our expectation of further funding of this account has not materialized after several months.) The following figures describe the results of our efforts on the other cases to date.

A.1.1 LOW CURRENT: $I_b = 22.5$ kA (e.g., $r_b = 49$ cm and $n_b = 10^9$ cm^{-3})

We begin our series of runs using the particle-in-cell code, ISIS 5.0, developed at Los Alamos National Laboratory. Results and parameters used in this series can be found in Table A–1. Since we were running ISIS at the Weapons Laboratory for the first time, we felt it was necessary to rerun a previous case to insure the validity of future results. We chose LANL run AM ($I_b = 22.5$ kA) as our comparison case.[1] Changing the run ID to AA (Table A–1), we reran the simulation and got very good agreement with the previous LANL case AM (Figs. A–1a–A–3a). Since the amount of smoothing used affects the codes' run time, run AB was built by turning-off the smoothing in X1 and X2 (NSM1 = 0 and NSM2 = 0). The results from run AB were very noisy and considered unusable (Figs. A–1b–A–3b). Although the results from run AB were not good, it did show us that smoothing in the radial direction was crucial and had to be used to reduce noise. Run AL was created from run AA by reducing the number of axial cells to NX1 = 2 and turning-off the axial smoothing (NSM1 = 0), but setting the radial smoothing to NSM2 = 3. While the results were a bit noisy (Figs. A–1c–A–3c), the run time improved by a factor of 34 as compared to run AA. Some of the noise in run AL might be attributed to the fact that only one slice was plotted for the field plots, while five slices were plotted for runs AA and AB. In Fig. A–3, run AL had only two cells for the axial integration. Runs AA, AB and AL all ran to $ct = 3000$ cm and appeared to be in a steady state (see Fig. A–16). A time-average current profile versus radius for the $I_b = 22.5$ kA cases can be found in Fig. A–4. The three runs exhibit nearly identical time-averaged behavior.

Because of the fast running time of run AL, it was felt a parameter study could be done quickly and efficiently using this case. Nine runs were created (AC–AK) by varying different parameters and running each case to $ct = 400$ cm (Table A–1). The results from these runs show little or no change versus run AL at this early time and were not included in this report.

A.1.2 MODERATE-CURRENT: $I_b = 452$ kA (e.g, $r_b = 49$ cm and $n_b = 2 \times 10^{10}$ cm^{-3})

For the $I_b = 452$ kA runs in this series, we used run AP (previously ran at LANL) as our base case.[1] All runs in this series (BA1, BC–BG, BI) used two axial cells, except for run BA2, which used four axial cells. Simulation runs in this series were carried out to different times. While most runs were carried out to either $ct = 1600$ cm or $ct = 2000$ cm, several runs ran only to $ct = 400$ cm. Figures A–5a–A–7h show B_0 versus r, E_r versus r, and axially-integrated J_z versus r for comparing runs (BA1–BA2, BC–BG, BI) at $ct = 400$ cm, while Figs. A–8a–A–10f show the same type of plots comparing runs (BA1–BA2, BC–BF) at later times ($ct = 1600$ cm and $ct = 2000$ cm). Results and parameters for these runs can be found in Table A–1. For this current, a steady state for the net current is reached at about $ct \approx 800$ cm (see Fig. A–17).

Run BA1 was the first run in the series and was used to compare with LANL run AP.[1] The results of BA1 were much noisier than AP (Figs. A–5a–A–10a). Run BA2 was built from BA1 by changing $IQ = 2$ to $IQ = 1$ (the IQ parameter is the integer iteration count for subcycling the particles; higher numbers resolve cyclotron motion better) and increasing the number of axial cells to NX1 = 4. Also the radial smoothing was turned-off (NSM2 = 0). By comparing BA1 (Figs. A–5a–A–10a) to BA2 (Figs. A–5b–A–10b) it shows the importance of having $IQ \geq 2$ and the need for radial smoothing (NSM2 > 0). Run BC was setup by increasing the number of axial particles per cell. The results from run BC (Figs. A–5c–A–10c) are quieter than run BA1 (Figs. A–5a–A–10a) and shows that increasing the number of axial particles per cell will help reduce noise. Run BD was created by modifying run BC to become a "hollow-beam" case, that is no particles were allowed in the first row of cells along the axis. The results of run BD (Figs. A–5d–A–10d) show little or no improvement using the hollow-beam. Run BE was generated by reducing the axial and radial cell size from 0.2 cm to 0.15 cm. The results from run BE (Figs. A–5e–A–10e) are quieter than run BC (Figs. A–5c–A–10c) and indicate the need for a reduced cell size. Most runs to this point used radial smoothing (NSM2 = 3), but had the axial smoothing turned-off (NSM1 = 0). Run BF (Figs. A–5f–A–10f) was built from run BE (Figs. A–5e–A–10e) by setting NSM1 = 1, and the results showed a slight noise reduction by using axial smoothing. Feeling that the best way to continue to reduce noise was to increase the number of axial and radial particles per cell, run BG was created in this manner. By comparing the results of run BG (Figs. A–5g–A–7g) to run BC (Figs. A–5c–A–7c), it is apparent that increasing the number of particles per cell does reduce noise. Run BI (Figs. A–5h–A–7h) was built from run BG (Figs. A–5g–A–7g) by decreasing the number of axial particles per cell by one half. The results showed an increase in noise and further proves the importance of having a sufficiently large number of axial particles per cell. Comparing run BI (Figs. A–5h–A–7h) with run BA1 (Figs. A–5a through

A–7a) shows the importance of having a sufficiently large number of radial particles per cell. Figure A–11 shows time-average current profiles for runs (BA1–BA2, BC–BF) which ran to times ≥ 1600. Again, all the runs exhibit nearly identical time-averaged behavior, except for run BA2.

A.1.3 HIGH CURRENT: $I_b = 1808$ kA (e.g., $r_b = 49$ cm and $n_b = 8 \times 10^{10}$ cm^{-3})

Only one run was made at I_b = 1808 kA before the Weapons Laboratory account expired. Run BB (Figs. A–12a–A–12f) ran out to ct = 2000 cm. The net current appeared to reach a steady state at about $ct \approx 400$ cm (see Fig. A–18). This run had $IQ = 1$ and too few particles per cells radially, and the results looked similar to runs BA1 (Figs. A–5a–A–10a) and BA2 (Figs. A–5b–A–10b) in quality. Because of the extreme noise, the only results that were of much use was the time average current profile (Fig. A–13) taken at ct = 2000 cm.

A.1.4 CONCLUSION

It is apparent that several parameters have a great influence on reducing the amount of noise in a run. Having the axial and radial smoothing (NSM1 and NSM2) turned-on is crucial to noise reduction, and also IQ (the integer iteration count for subcycling particles) must be set to a value ≥ 2. The reduction in cell size was important in improving the simulation results. Having a sufficiently large number of particles per cell appears to have had the most noticeable effect of all.

The scaling of the current radial-profile and the net current is summarized in two figures. Figure A–14 shows the time average current profile for different values of the beam current, and Fig. A–15 shows the net current as it scales to the square root of the beam current.

Figures A–16a–A–16b show a good comparison of the effect that the number of axial cells has on the noise in a simulation. Figure A–16a is a time history and frequency spectrum of the net current for run AA with 129 axial cells with a beam current of 22.5 kA. Figure A–16b is a time history and frequency spectrum of the net current for run AL with two axial cells with a beam current of 22.5 kA. After examination one can see that the number of axial cells has only a slight effect on the noise. Figures A–17 and A–18 show time history and frequency spectrum of the net current for beam currents of 452 kA (run BF) and 1808 kA (run BB). These figures show that the noise increases as the beam current increases unless more cells and particles are used. The net current values used in Figs. A–14–A–15 were taken from the time history plots shown in Figs. A–16–A–18. Figures A–16–A–18 also show that the net current reaches a steady state in a time of order $ct/r_b \sim 200c/\omega_{be}r_b$. Thus, the higher current runs may not have to be run as long. As a rough estimate, the number of CRAY hours to reach steady state appears to scale as $t_{run}(\mathrm{hr}) \sim 2(\omega_{be}r_b/13c)$ (NPC/40), where NPC is the number of particles per cell.

By taking an overall view of the runs done in $I_b = 452$ kA series, run BG (Figs. A–5g–A–7g) was giving the best results followed by run BI (Figs. A–5h–A–7h) at early times ($ct = 400$ cm). At later times ($ct \geq 1600$ cm) run BF (Figs. A–5f–A–10f) gave very good results. Again the major factor in all cases that returned reasonable results was that: (a) smoothing was turned-on, (b) IQ was set to at least two, (c) a sufficiently large number of particles per cell was used ($\gtrsim 40$).

In order to achieve results comparable with run BG (Figs. A–5g–A–7g) for 1808 kA, run BB (Figs. A–12a–A–12f) would have to have $IQ = 2$, DX1 = DX2 = 0.1 cm, six particles per cell axially and seven radially (42 total). A simulation with these parameter settings would take about 4 hours of Cray time to execute out to a time of $ct = 400$ cm.

TABLE A–1. SIMULATION RESULTS AND PARAMETERS.

Run Label	Cell Size DX (cm)	Axial Cells	Radial Cells	Axial Smoothing	Radial Smoothing	Time Step	Axial Particles Per Cell	Radial Particles Per Cell	Time Limit	Comments
I_b = 22.5 kA										
AA	1.0	129	55	4	4	0.5	4.0	1.8	3000	Benchmark, good comparison with LANL run AM
AB	1.0	129	55	0	0	0.5	4.0	1.8	3000	Very noisy, smoothing crucial
AL	1.0	2	55	0	3	0.5	6.0	1.8	3000	Somewhat noisy, still looks pretty good, only one slice plotted
AC	1.0	2	55	0	3	0.5	6.0	8.0	400	Too early in time, shows little or no change
AD	1.0	2	55	0	3	0.5	4.5	8.0	400	Too early in time, shows little or no change
AE	1.0	2	55	0	3	0.5	3.0	8.0	400	Too early in time, shows little or no change
AF	1.0	2	55	0	3	0.5	6.0	6.0	400	Too early in time, shows little or no change
AG	1.0	2	55	0	3	0.5	6.0	4.0	400	Too early in time, shows little or no change
AH	1.0	2	55	0	3	0.5	7.5	8.0	400	Too early in time, shows little or no change
AI	1.0	2	55	0	3	0.5	9.0	8.0	400	Too early in time, shows little or no change
AJ	1.0	2	55	0	3	0.5	10.5	8.0	400	Too early in time, shows little or no change
AK	1.0	2	55	0	3	0.5	12.0	8.0	400	Too early in time, shows little or no change
I_b = 452 kA										
BA1	0.2	2	277	0	3	0.1	3.0	0.88	2000	Looks okay, but needs more radial particles per cell
BA2	0.2	4	277	0	0	0.1	2.5	0.88	2000	Compared with BA1, shows that $IQ \geq 2$, also smoothing crucial
BC	0.2	2	277	0	3	0.1	5.0	1.76	2000	Compared with BA1, shows that more particles per cell is better
BD	0.2	2	277	0	3	0.1	5.0	1.76	2000	Like BC except hollow beam, no improvement
BE	0.15	2	370	0	3	0.085	5.0	1.76	1600	Compared with BC, shows smaller cells are better
BF	0.15	2	370	1	3	0.085	5.0	1.76	1600	Compared with BE, shows axial smoothing helps
BG	0.2	2	277	0	3	0.1	6.0	7.1	572	Compared with BC, shows further increase in particles continue to decrease noise
BI	0.2	2	277	0	3	0.1	3.0	7.1	400	Compared with BA1, shows more particle per cell in X2 decreases noise
I_b = 1808 kA										
BB	DX1 = 0.2 DX2 = 0.1	2	554	0	3	0.05	3.0	0.52	2000	Noisy, did not reach steady state, needs $IQ = 2$, DX1 = DX2 = 0.1, more particles per cell

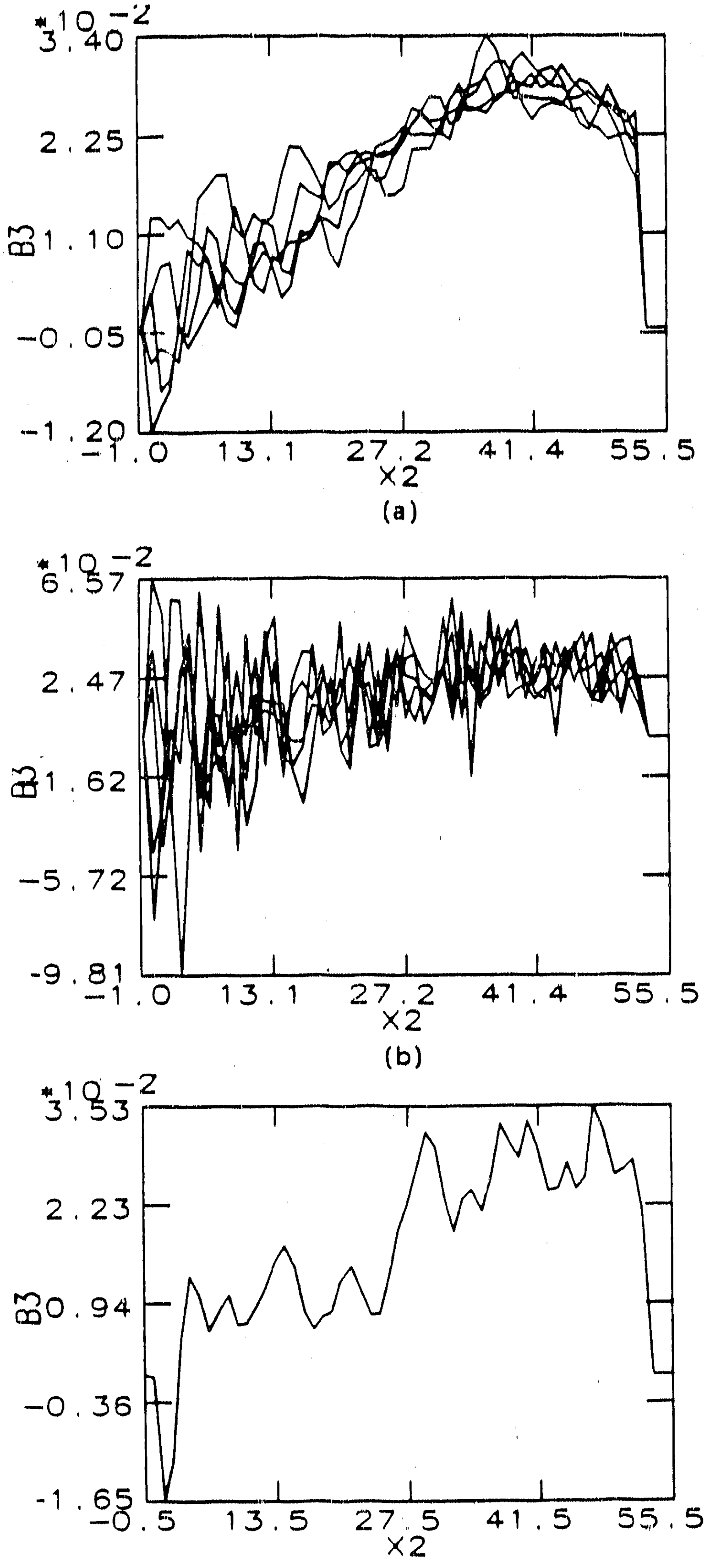

Figure A–1. Periodic simulation results comparing B_θ versus r at $ct = 3000$ cm for three runs with $I_b = 22.5$ kA. (a) run AA, (b) run AB, (c) run AL.

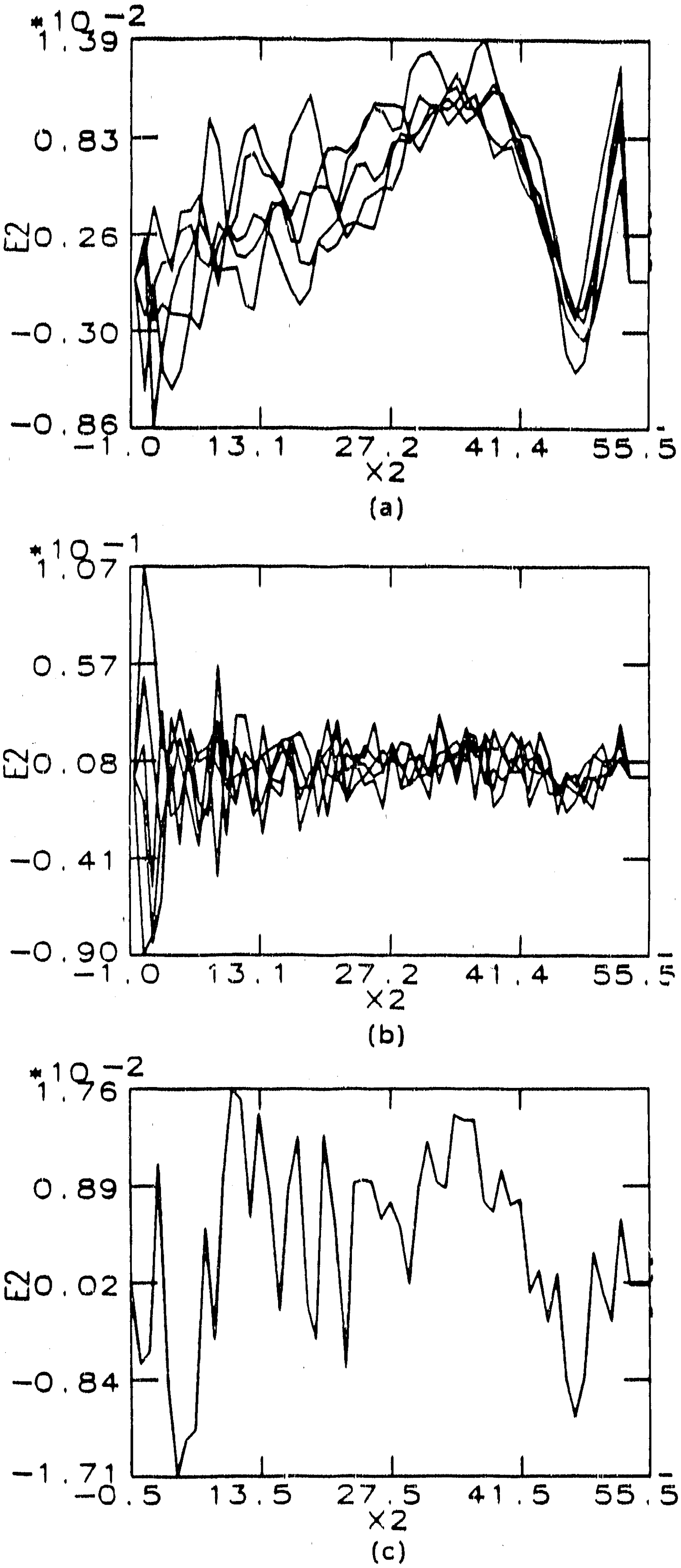

Figure A–2. Periodic simulation results comparing E_r versus r at $ct = 1000$ cm for three runs with $I_b = 22.5$ kA. (a) run AA, (b) run AB, (c) run AL.

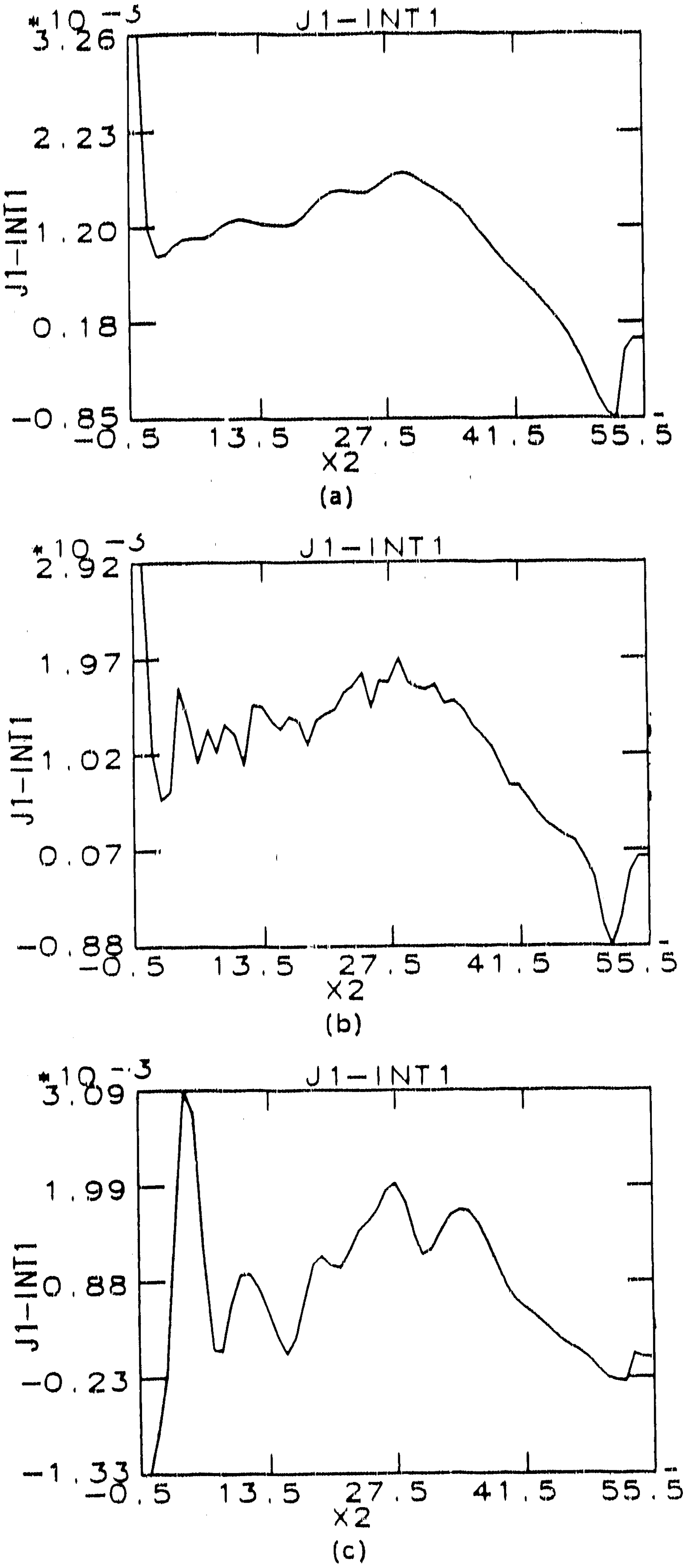

Figure A-3. Periodic simulation results comparing axially-integrated J_z versus r at ct = 3000 cm for three runs with I_b = 22.5 kA. (a) run AA, (b) run AB, (c) run AL.

LLNL PLASMOID PROPAGATION

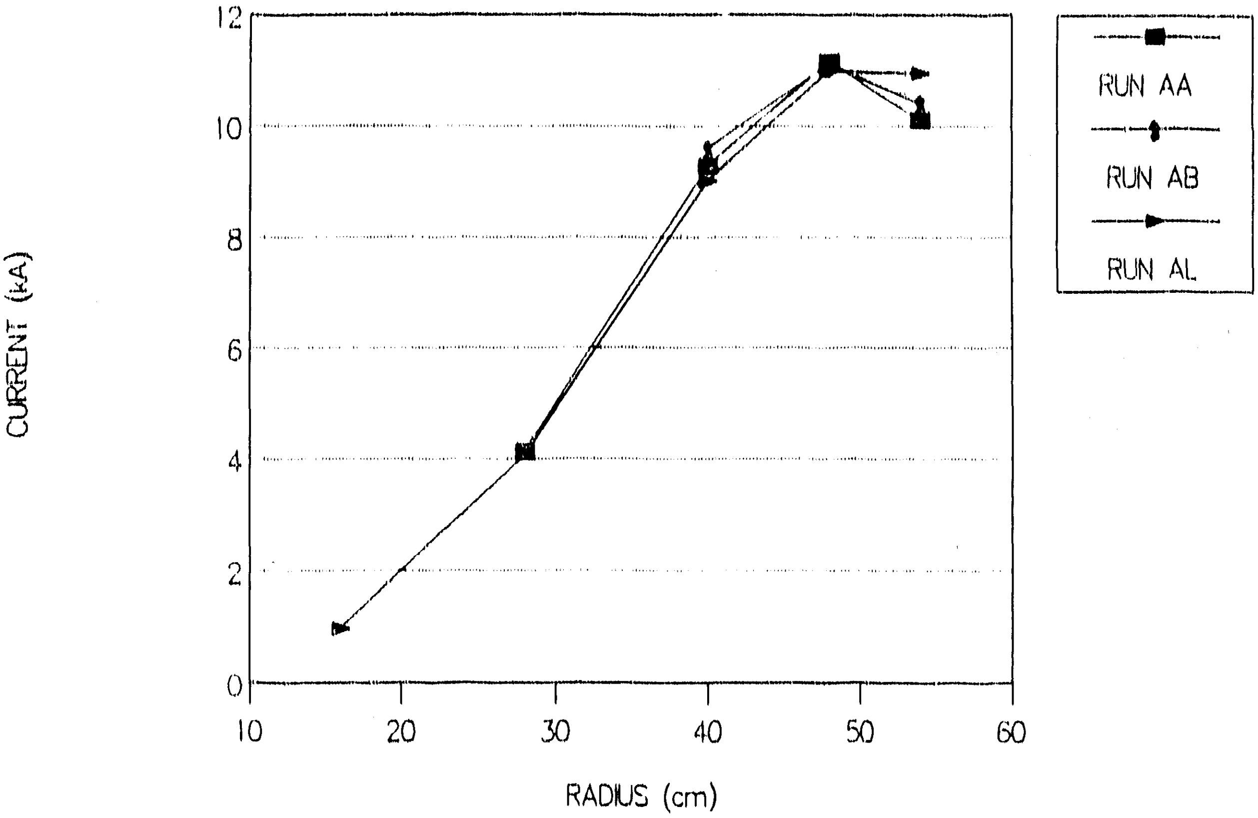

Figure A–4. Time averaged current profile in steady state for runs at $I_b = 22.5$ kA.

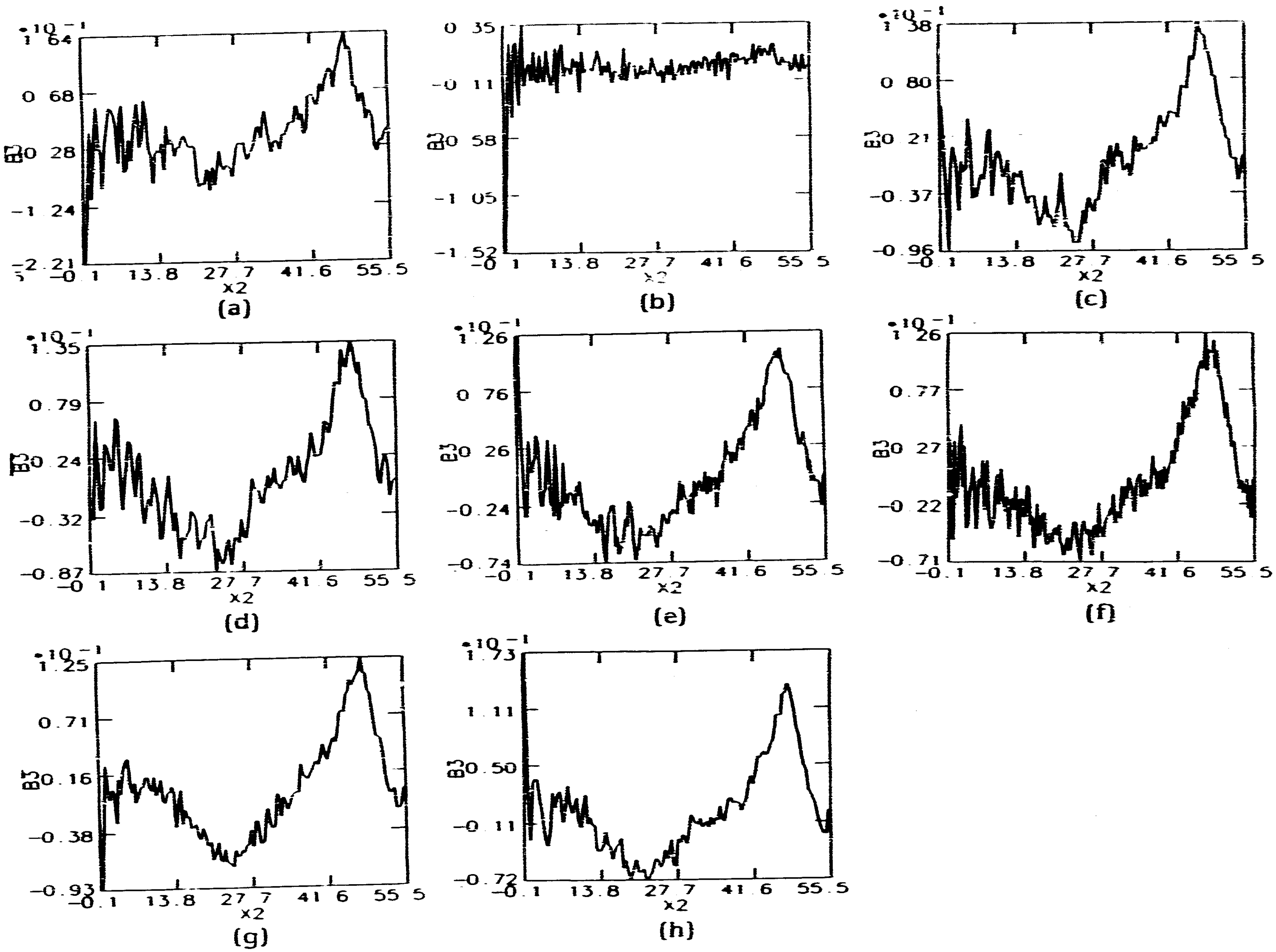

Figure A-5. Periodic simulation results comparing B_θ versus r at $ct = 400$ cm for eight runs with $I_b = 452$ kA. (a) run BA1, (b) run BA2, (c) run BC, (d) run BD, (e) run BE, (f) run BF, (g) run BG, (h) run BL

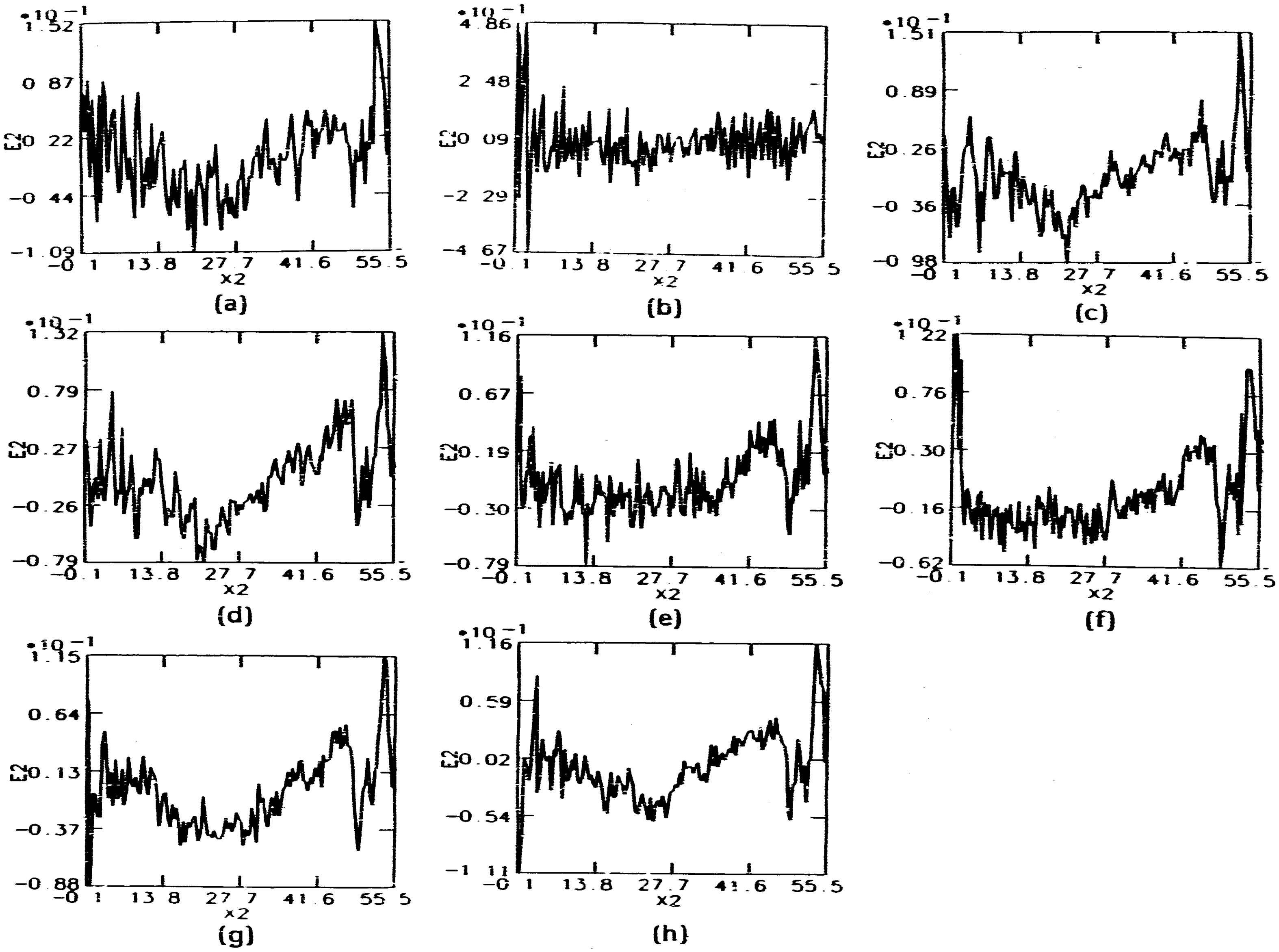

Figure A–6. Periodic simulation results comparing E_r versus r at $ct = 400$ cm for eight runs with $I_b = 452$ kA. (a) run BA1, (b) run BA2, (c) run BC, (d) run BD, (e) run BE, (f) run BF, (g) run BG, (h) run BI.

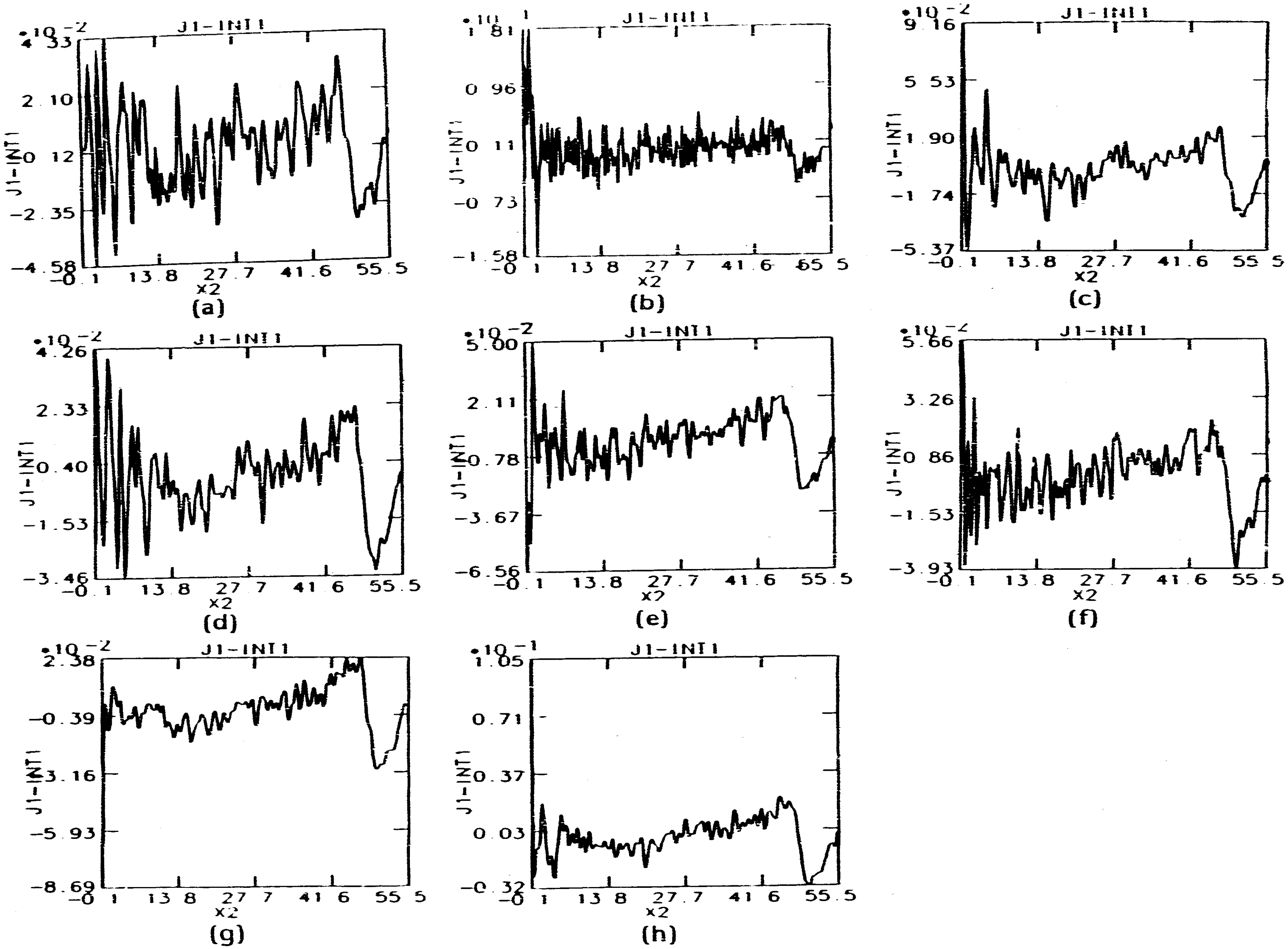

Figure A-7. Periodic simulation results comparing axially-integrated J_z versus r at $ct =$ 400 cm for eight runs with $I_b = 452$ kA. (a) run BA, (b) run BA1, (c) run BA2, (d) run BC, (e) run BD, (e) run BE, (f) run BF, (g) run BG, (h) run BI.

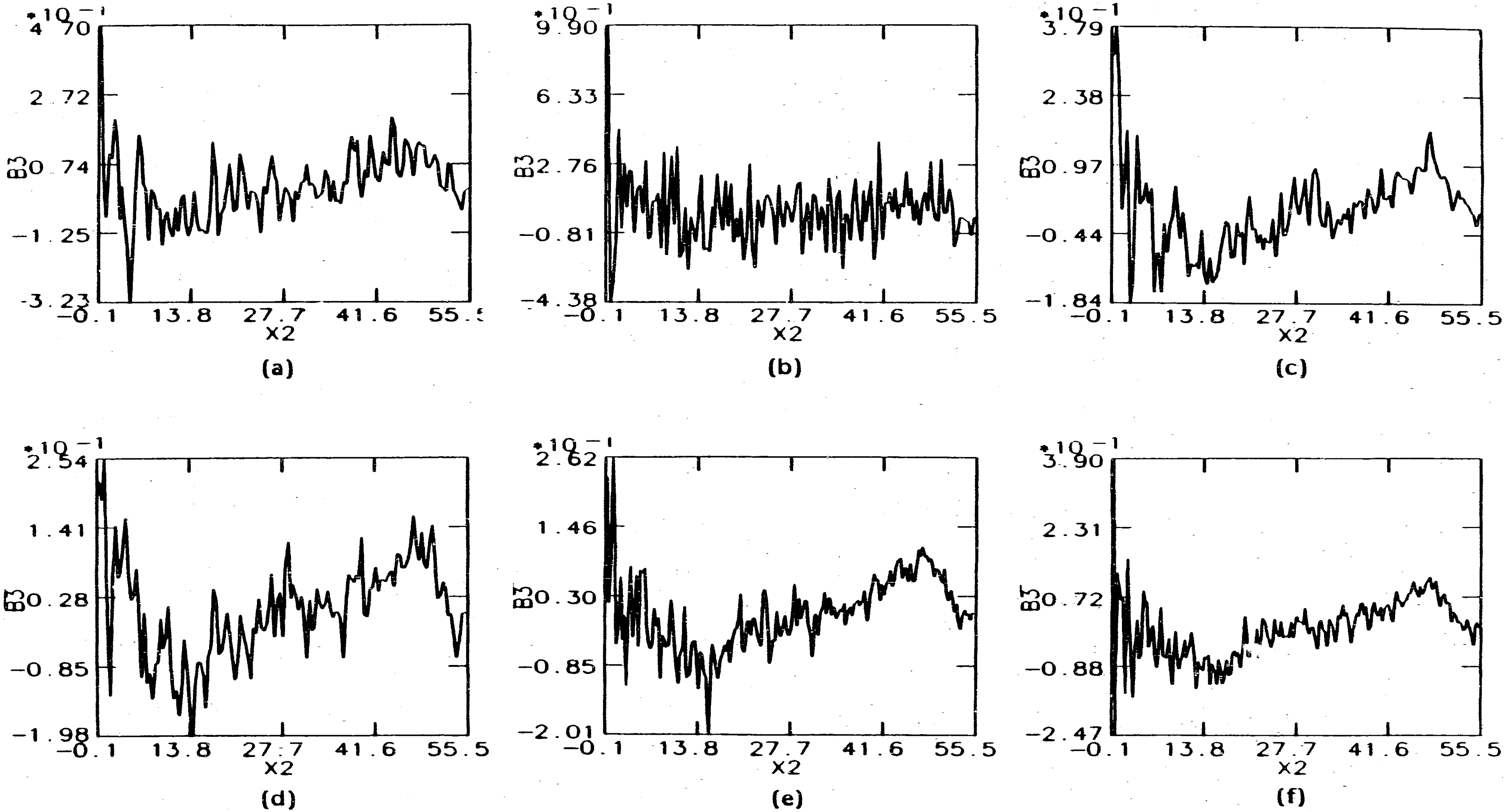

Figure A-8. Periodic simulation results comparing B_θ versus r at late times for six runs with $I_b = 452$ kA. (a) run BA1 at $ct = 2000$ cm, (b) run BA2 at $ct = 2000$ cm, (c) run BC at $ct = 2000$ cm, (d) run BD at $ct = 2000$ cm, (e) run BE at $ct = 1600$ cm, (f) run BF at $ct = 1600$ cm.

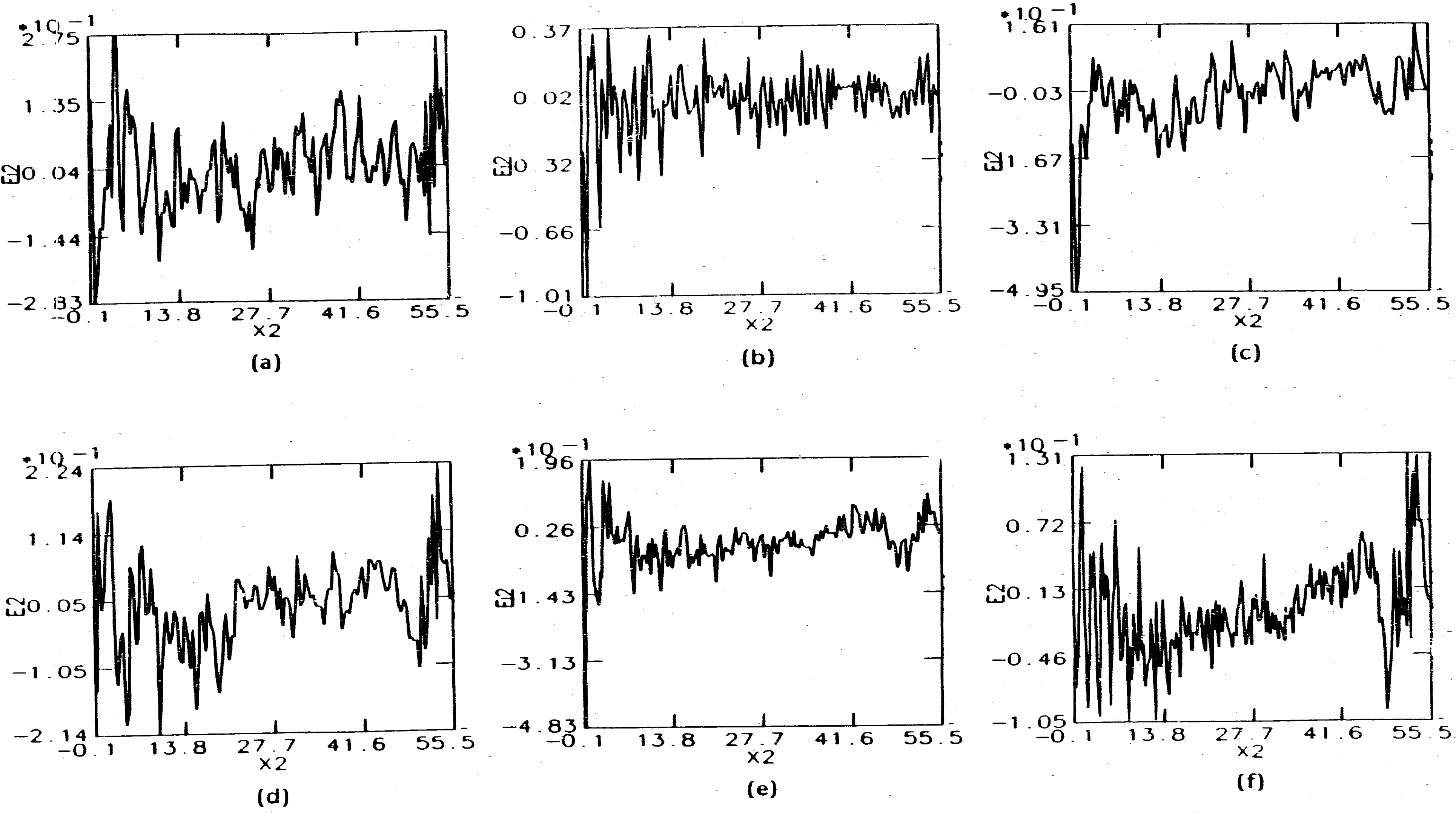

Figure A-9. Periodic simulation results comparing E_r versus r at late times for six runs with $I_b = 452$ kA. (a) run BA1 at $ct = 2000$ cm, (b) run BA2 at $ct = 2000$ cm, (c) run BC at $ct = 2000$ cm, (d) run BD at $ct = 2000$ cm, (e) run BE at $ct = 1600$ cm, (f) run BF at $ct = 1600$ cm.

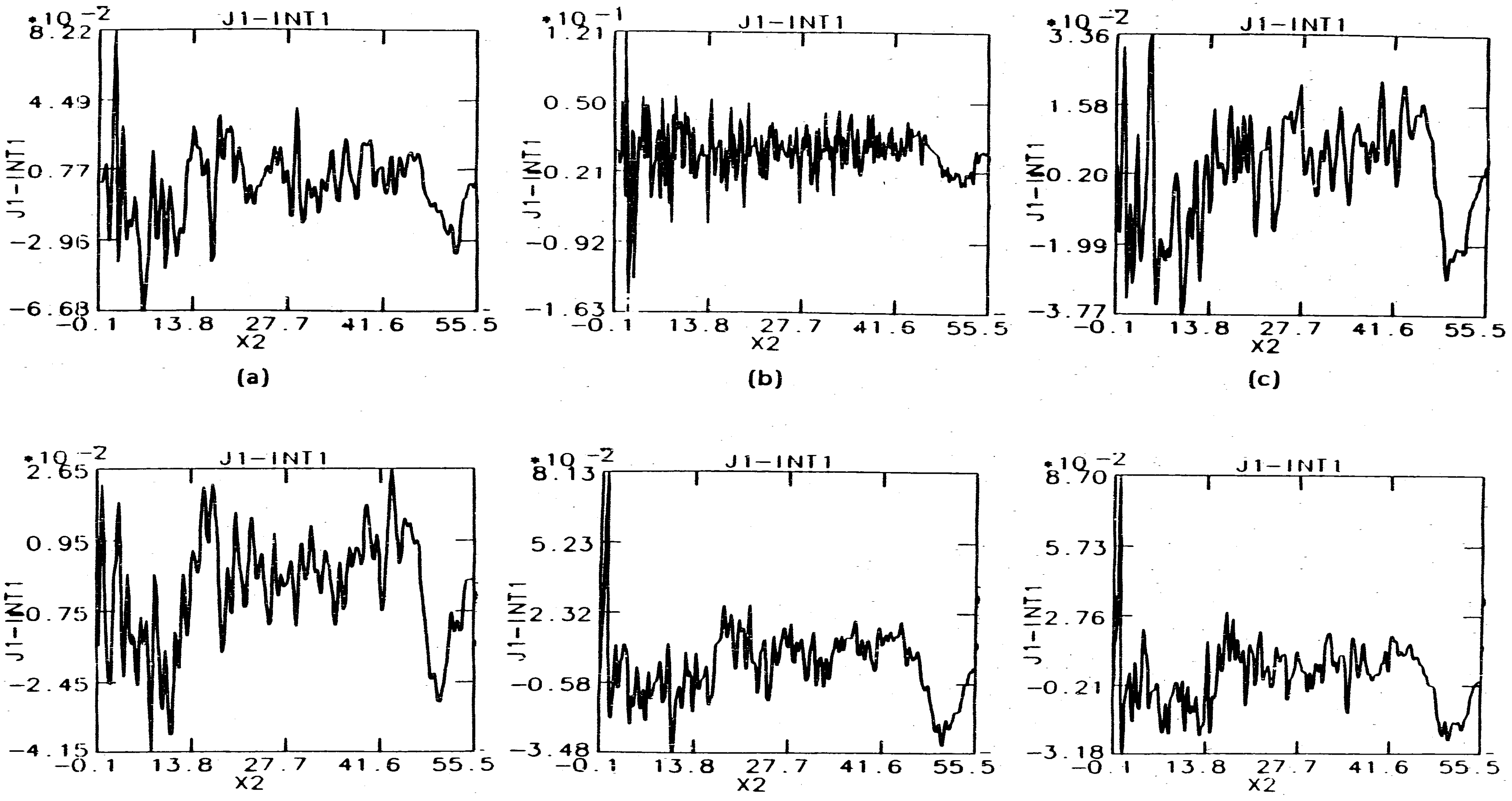

(a) (b) (c)

(d) (e) (f)

Figure A-10. Periodic simulation results comparing axially-integrated J_z versus r at late times for six runs with $I_b = 452$ kA. (a) run BA1 at $ct = 2000$ cm, (b) run BA2 at $ct = 2000$ cm, (c) run BC at $ct = 2000$ cm, (d) run BD at $ct = 2000$ cm, (e) run BE at $ct = 1600$ cm, (f) run BF at $ct = 1600$ cm.

LLNL PLASMOID PROPAGATION

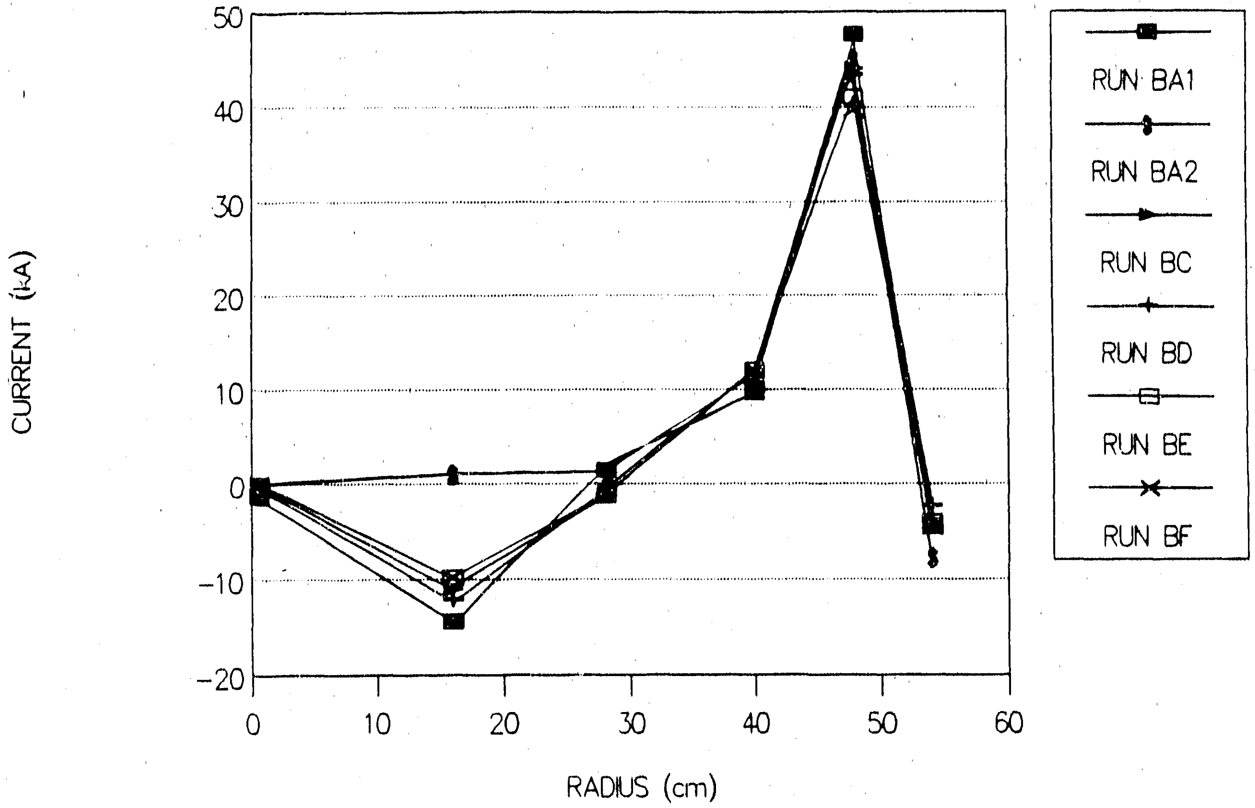

Figure A–11. Time averaged current profile in steady state for runs at $I_b = 452$ kA.

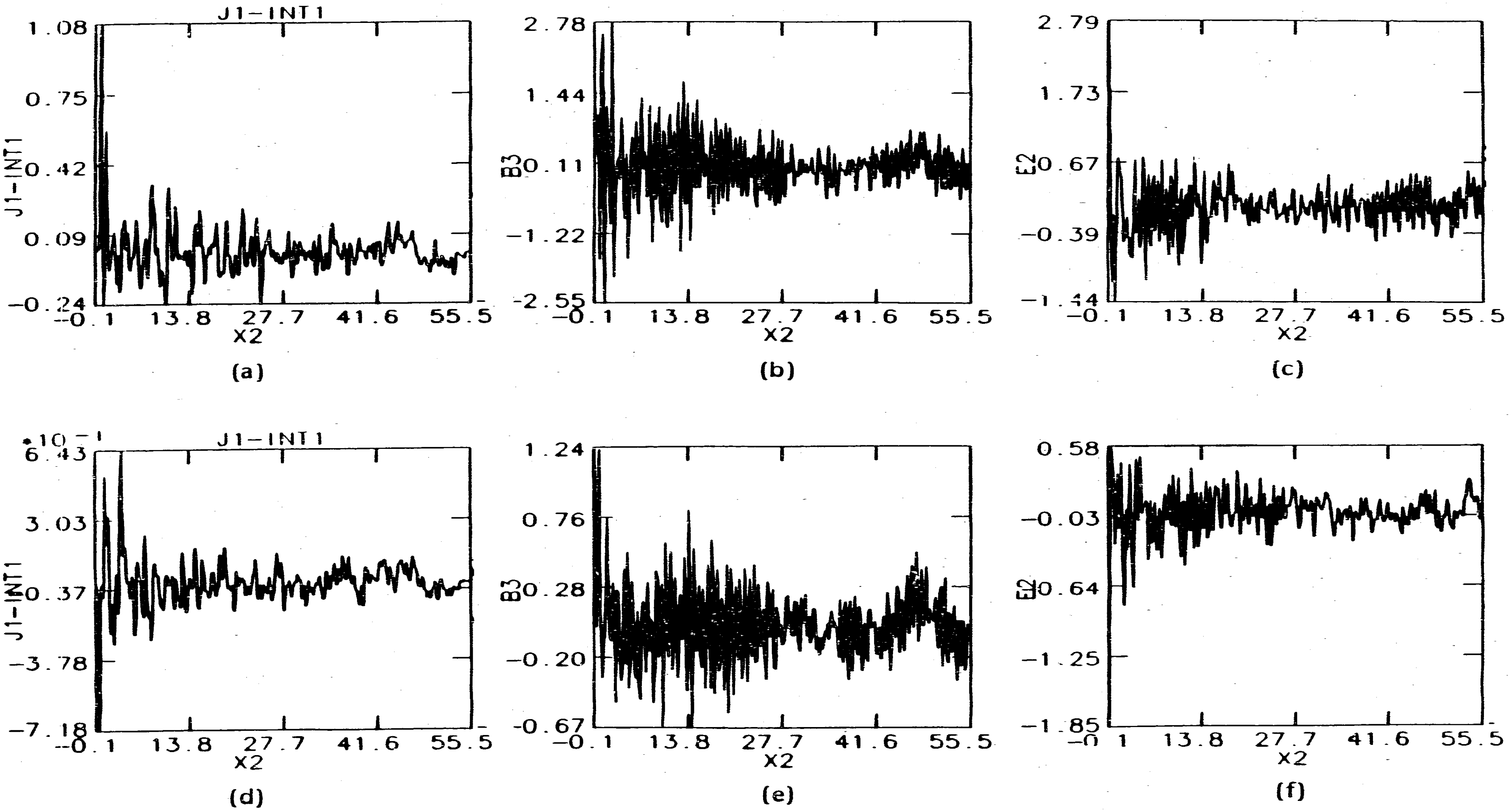

Figure A–12. Periodic simulation BB at late and early times for $I_b = 1808$ kA. (a) axially-integrated J_z versus r at $ct = 2000$ cm, (b) B_θ versus r at $ct = 2000$ cm, (c) E_r versus r at $ct = 2000$ cm, (d) axially-integrated J_z versus r at $ct = 400$ cm, (e) B_θ versus r at $ct = 400$ cm, (f) E_r versus r at $ct = 400$ cm.

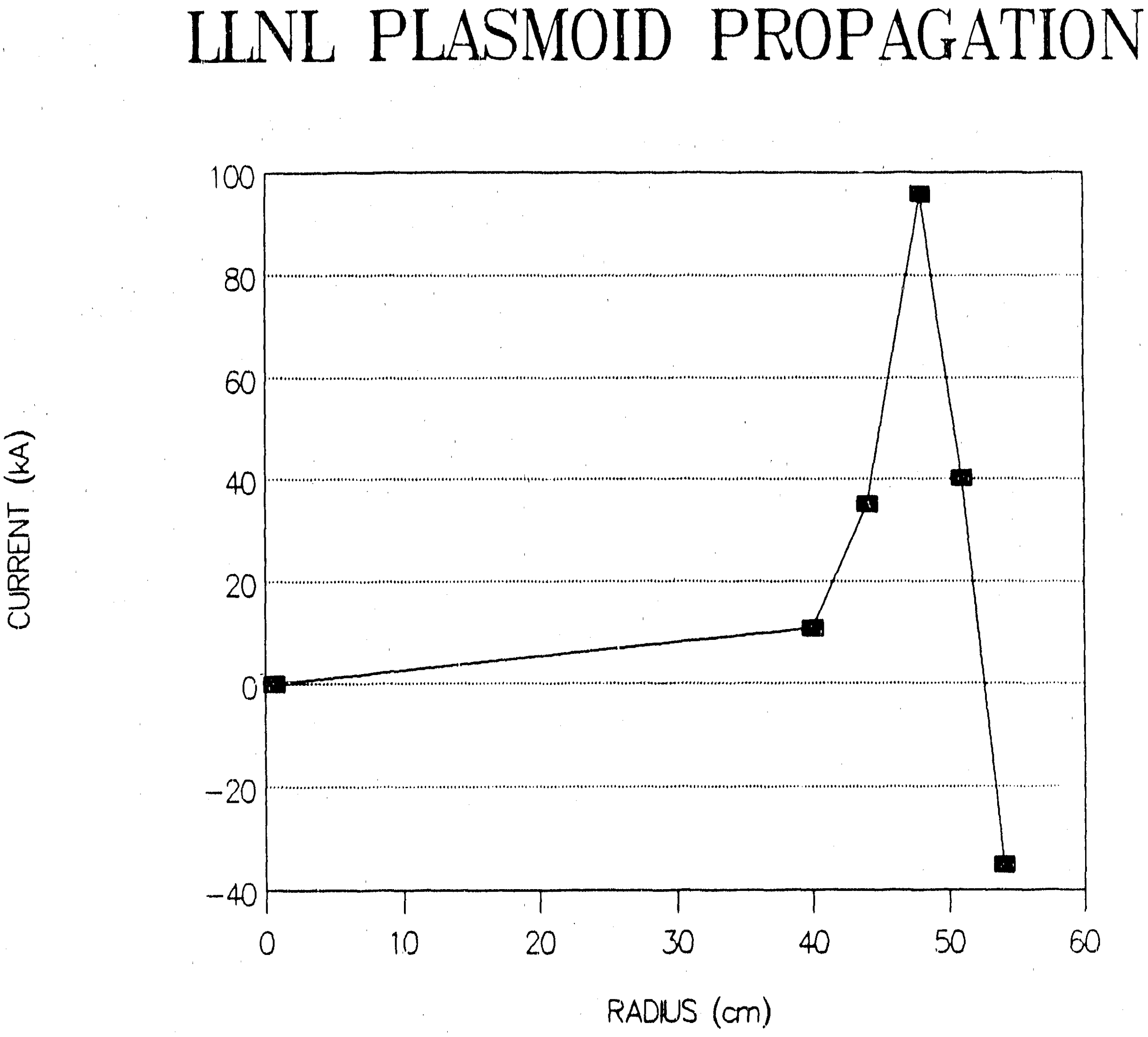

LLNL PLASMOID PROPAGATION

Figure A–13. Time averaged current profile for run BB near end of run with $I_b = 1808$ kA.

LLNL PLASMOID PROPAGATION

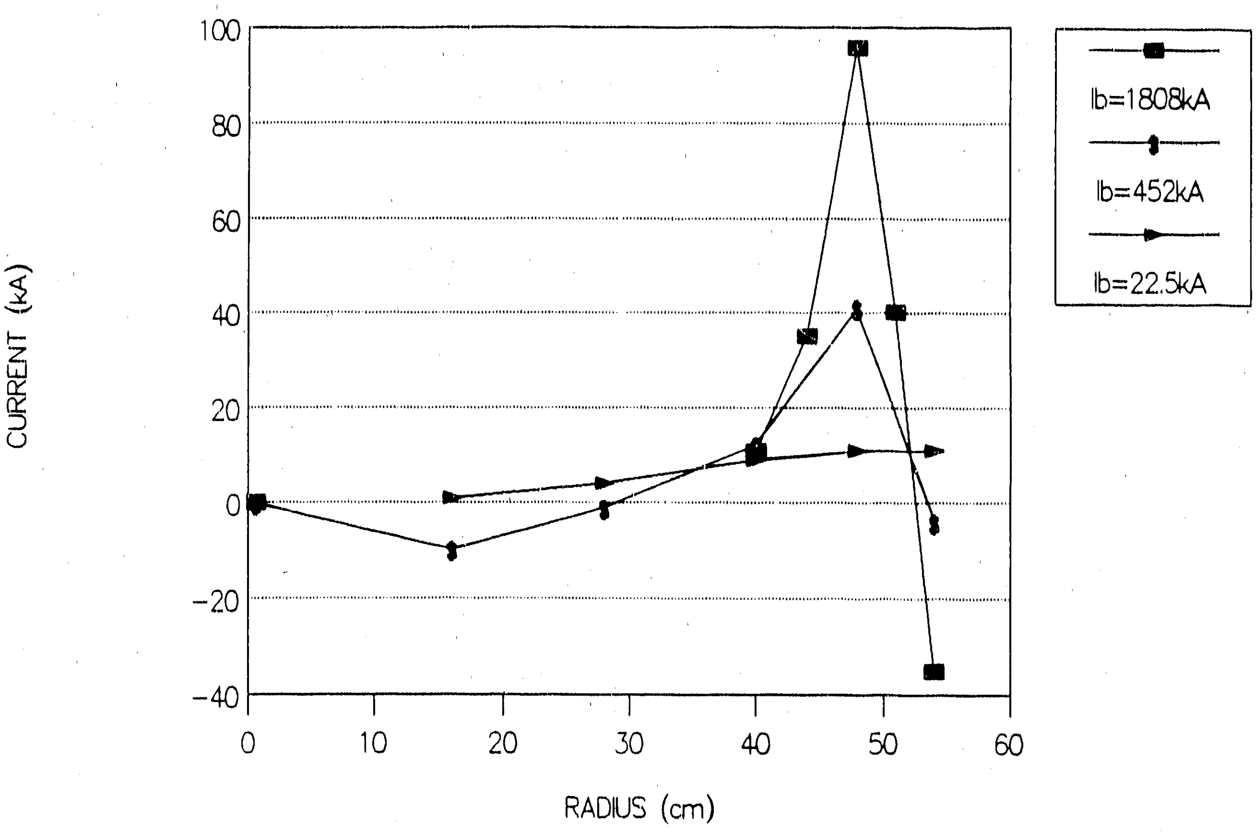

Figure A-14. Time averaged current profile comparing different I_b for three runs.

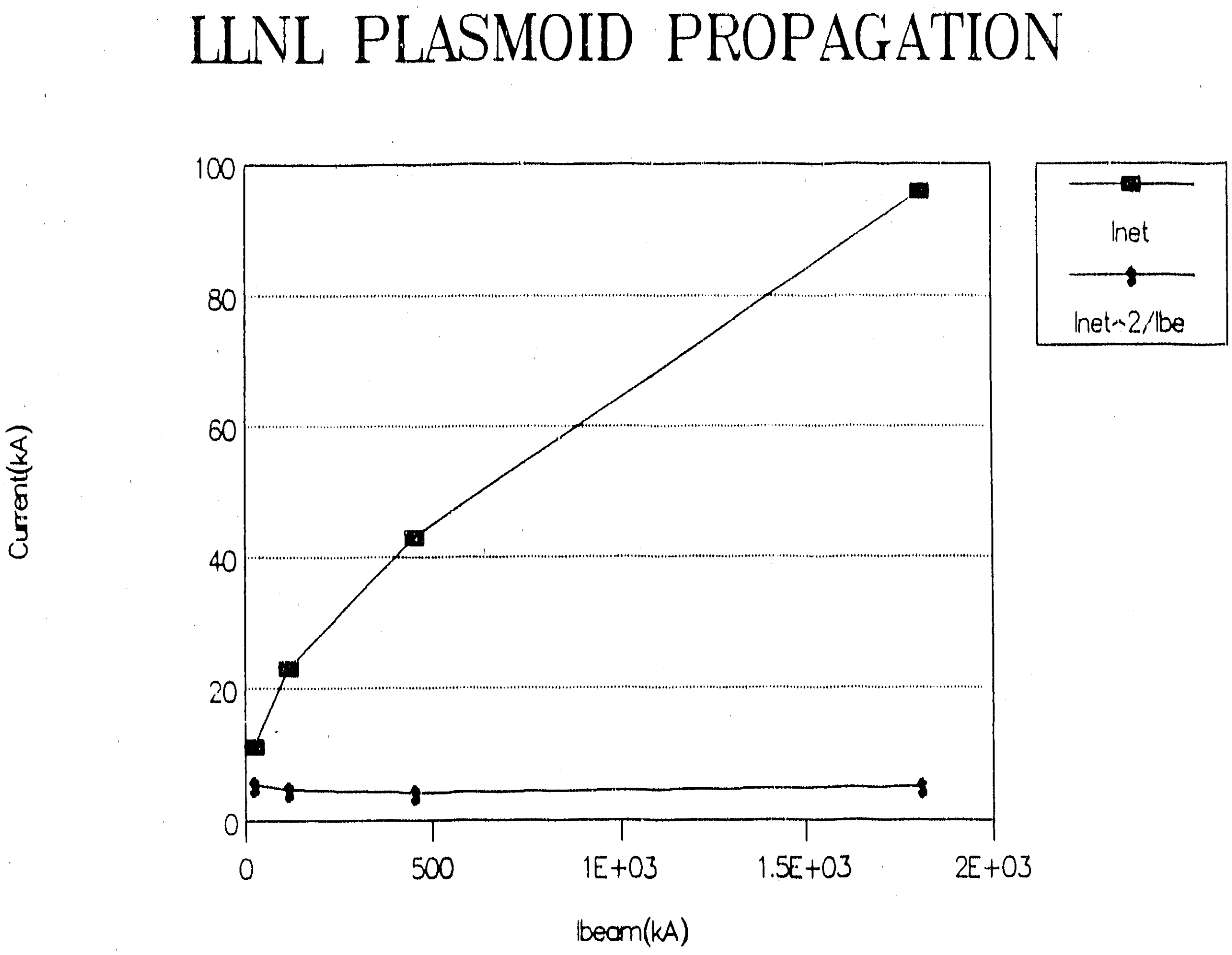

Figure A-15. Net current as it scales to the square root of beam current.

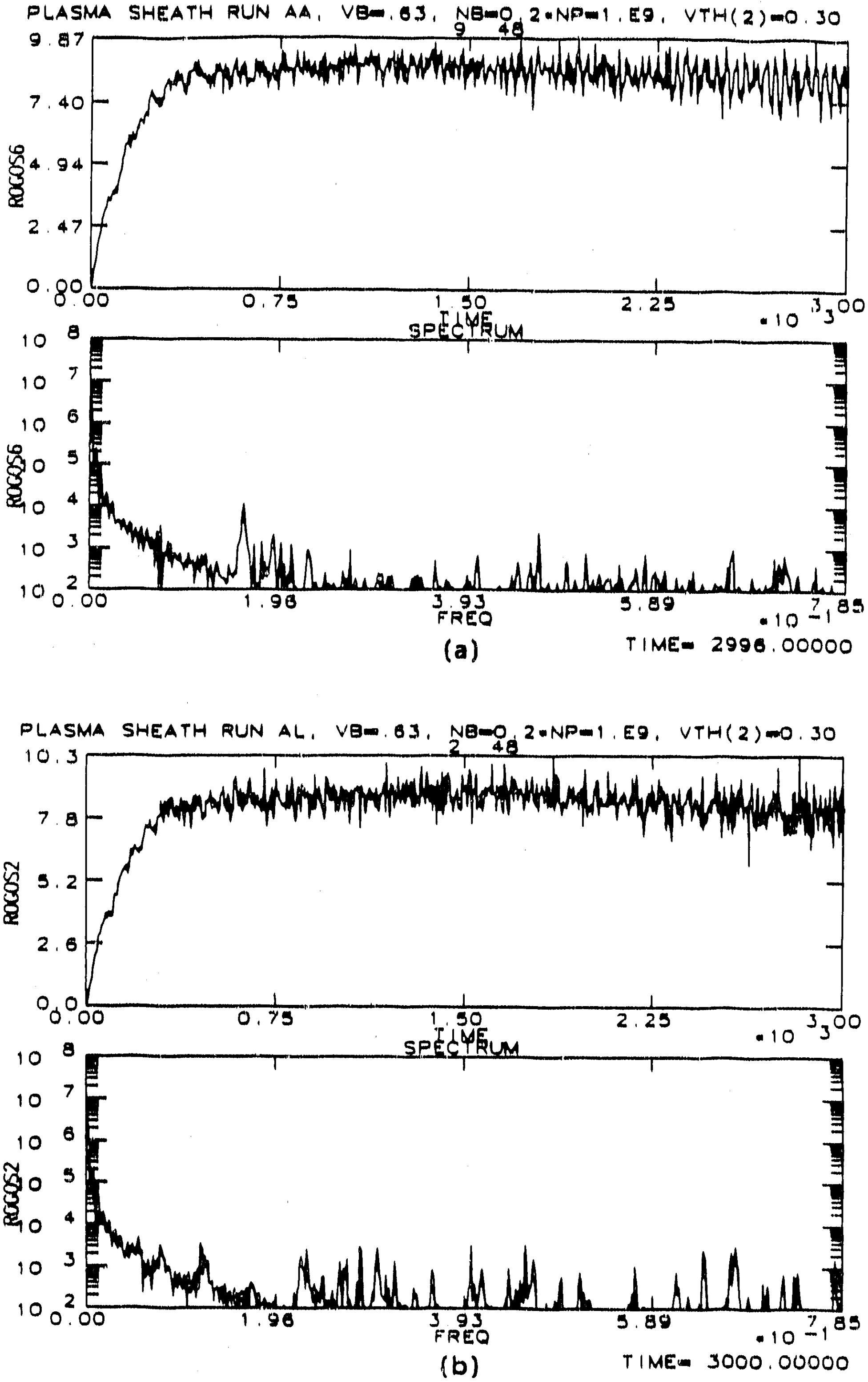

Figure A-16. Periodic simulation results comparing time history and frequency spectrum of the net current for two runs with a different number of axial cells. $I_b = 22.5$ kA. Current in units of 1.35 kA, frequency in units of $\omega_0 = 3 \times 10^{10}$ rad/s. (a) run AA with 129 axial cells, (b) run AL with two axial cells.

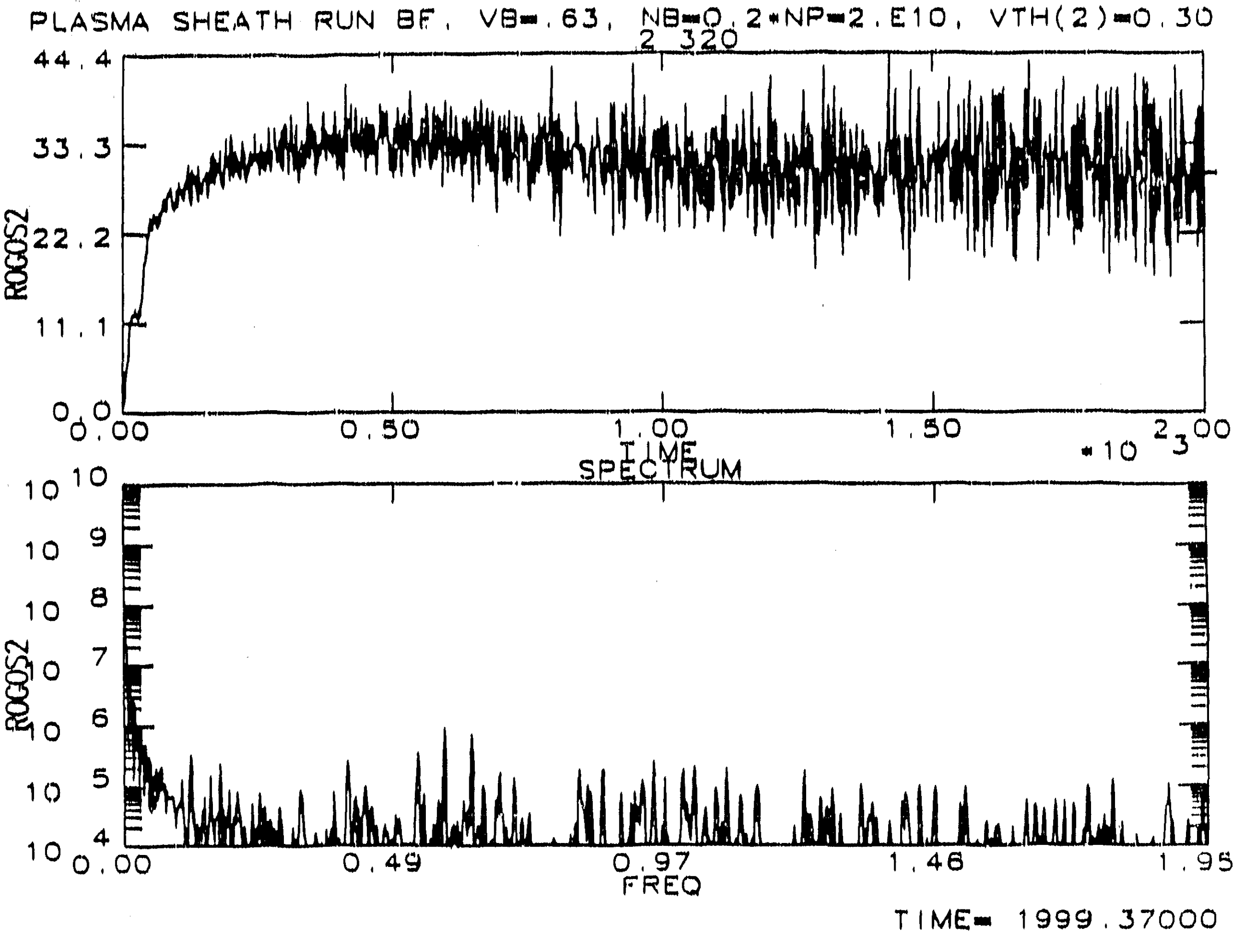

Figure A–17. Periodic simulation BF, time history and frequency spectrum of the net current. I_b = 452 kA. Current in units of 1.35 kA, frequency in units of $\omega_0 = 3 \times 10^{10}$ rad/s.

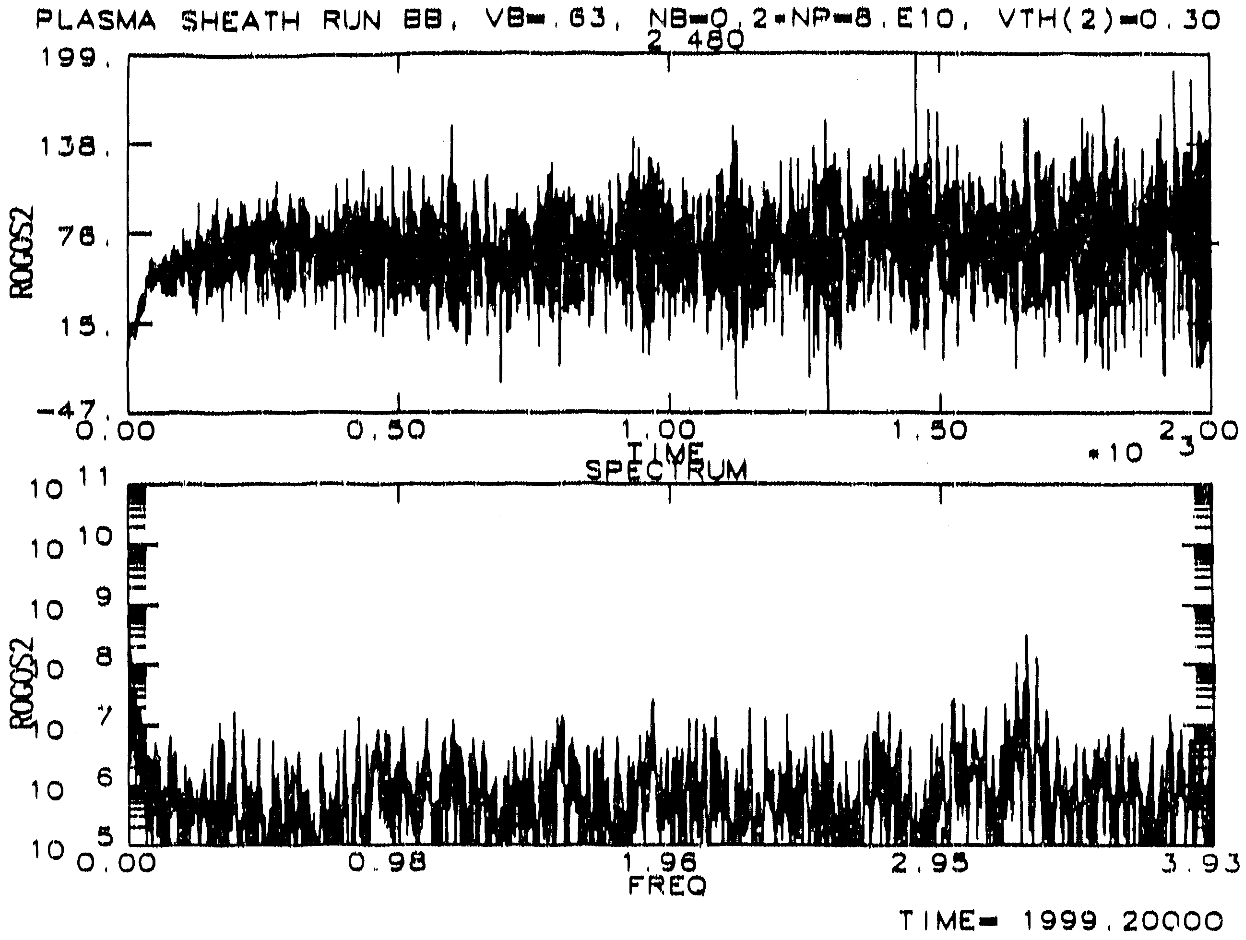

Figure A–18. Periodic simulation BB, time history and frequency spectrum of the net current. $I_b = 1808$ kA. Current in units of 1.35 kA, frequency in units of $\omega_0 = 3 \times 10^{10}$ rad/s.

END

DATE FILMED

10 / 31 / 90